

Medical Imaging

*Thomas Szabo, PhD**

OUTLINE

16.1 Introduction	1040	16.7 Image Fusion	1106
16.2 Diagnostic Ultrasound Imaging	1042	16.8 Summary	1107
16.3 Magnetic Resonance Imaging	1071	16.9 Exercises	1108
16.4 Magnetoencephalography	1099	References	1110
16.5 Contrast Agents	1101	Suggested Readings	1110
16.6 Comparison of Imaging Modes	1103		

AT THE CONCLUSION OF THIS CHAPTER, STUDENTS WILL BE ABLE TO:

- Distinguish between the principles of pulse-echo ranging and ultrasound imaging.
- Describe how ultrasound images are formed.
- Explain the fundamentals of acoustic wave propagation, reflection, and refraction.
- Describe the operation and characteristics of a piezoelectric transducer.
- Explain the principle of an acoustic matching layer.
- Discuss the basic types of acoustic scattering.
- Calculate the effects of acoustic absorption.
- Describe the fundamentals of beam formation and focusing.
- Discuss the block diagram of an ultrasound imaging system.
- Explain basic ultrasound Doppler.
- Explain four basic principles of the interaction of magnetic fields and charges.
- Discuss spin states and precession of nuclear dipoles in a magnetic field.

*With contributions from Kirk K. Shung and Steven Wright.

- Explain the Larmor frequency and nuclear magnetic resonance.
- Explain how flip angles affect recovery and relaxation time constants.
- Distinguish between free induction decay and spin echo signals.
- Explain how detected resonance signals are spatially localized.
- List the steps involved in creating a magnetic resonance image.
- Explain what is displayed in a magnetic resonance image.
- Draw and explain the block diagram of an MRI system.
- Explain the significance of k-space in MRI.
- Discuss applications of MRI including fMRI.
- Discuss the principles of magneto-encephalography.
- Compare contrast agents for different imaging modalities.
- Explain image fusion.
- Compare major imaging modalities.

16.1 INTRODUCTION

Of the major diagnostic imaging modalities, ultrasound is the most frequently used, second only to standard plane-view x-rays. Over the years, the cumulative number of ultrasound exams completed is estimated to be in the billions. Unlike x-rays and computed tomography (CT) scanning, ultrasound imaging involves no ionizing radiation and therefore is considered to be noninvasive. Furthermore, it is portable, easy to apply, low in cost, and provides real-time diagnostic information about the mechanical nature and motion of soft tissue and blood flow. The basic principle of ultrasound imaging is the display of pulse-echoes backscattered from tissues.

Magnetic resonance imaging (MRI) also obtains detailed anatomic information without using ionizing radiation. MRI differentiates among types of organs by sensing the spin of their atoms when a person is placed in a large, static, magnetic field. Static cross-sectional images of the body include both bone and soft tissue, and the appearance of the images can vary considerably by the selection of specific parameters. Of the major imaging modalities, MRI is the most abstract and complicated technically. In addition to its precise anatomical capability, it is often used for presurgery planning and for cancer detection. Functional MRI (fMRI) provides images of brain activity in response to various stimuli.

In this chapter, the operation and principles of both ultrasound imaging and MRI will be explained. At the end of the chapter, the main features of all major imaging modalities, including CT and x-ray, will be compared. An understanding of the basic principles of the Fourier transform, introduced in Chapter 10, will enhance comprehension of the imaging concepts introduced in this chapter. More information about the Fourier transform is provided in the next section.

16.1.1 Review of Fourier Transforms

Because Fourier transforms simplify the understanding of the imaging principles of ultrasound imaging and MRI, their relevant properties are reviewed here. One important Fourier transform concept from Chapter 6 is the equivalence of convolution in the time

domain and multiplication in the frequency domain. Another is the use of an impulse response function and a transfer function for describing system and filter responses in the time and frequency, respectively.

An impulse function is a generalized function that has the unusual property that it samples the integrand:

$$\int_{-\infty}^{\infty} \delta(t - t_0) g(t) dt = g(t_0) \quad (16.1)$$

When the transform of the impulse function is taken, the result is an exponential

$$H(\omega) = \int_{-\infty}^{\infty} \delta(t - t_0) e^{-i\omega t} dt = e^{-i\omega t_0} \quad (16.2)$$

which shows that a delay in time is equivalent to a multiplicative exponential delay factor in the frequency domain. When the impulse has no delay or $t_0 = 0$, $H(\omega) = 1.0$, a constant.

The preceding relation can be generalized to the form where \mathcal{I} represents the Fourier transform operation,

$$\mathcal{I}[g(t - b)] = e^{-i2\pi b f} G(\omega) \quad (16.3)$$

A scaling factor can be added to this time shifting/delay theorem to make it even more useful,

$$\mathcal{I}[g(a(t - b))] = \frac{e^{-i\omega b}}{|a|} G(\omega/a) \quad (16.4a)$$

Note that a similar relation exists for the inverse transform denoted by \mathcal{I}^{-1} ,

$$\mathcal{I}^{-1}[G(a(\omega - b))] = \frac{e^{-ibt}}{|a|} g(t/a) \quad (16.4b)$$

Finally, an important unique property of the impulse function is

$$\delta(at) = \frac{1}{|a|} \delta(t) \quad (16.5)$$

EXAMPLE PROBLEM 16.1

Find the inverse Fourier transform of $R(\omega) = \sin[3(\omega - \omega_0)t_1]$.

Solution

Recognize the basic function G in $R(\omega)$ as

$$G(\omega) = \sin \omega t_1 = \frac{e^{i\omega t_1} - e^{-i\omega t_1}}{2i}$$

Continued

Then from the Fourier transform pair expressed in Eq. (16.2),

$$\mathfrak{F}^{-1}[G(\omega)] = g(t) = (i/2)[\delta(t - t_1) - \delta(t + t_1)]$$

From Eq. (16.4b) with $a = 3$ and $b = \omega_0$, find $r(t)$ as

$$\mathfrak{F}^{-1}[R(\omega)] = (e^{i\omega_0 t}/3)(i/2) \left[\delta\left(\frac{t - t_1}{3}\right) - \delta\left(\frac{t + t_1}{3}\right) \right]$$

and from scaling in the impulse function in Eq. (16.5),

$$r(t) = (e^{i\omega_0 t}) = (i/2)[\delta(t - t_1) - \delta(t + t_1)]$$

16.2 DIAGNOSTIC ULTRASOUND IMAGING

Diagnostic ultrasound imaging is the most widely used form of medical imaging. Its ability to reveal body structures and dynamics and blood flow in real time at low cost in a safe manner (using non-ionizing radiation) has expanded its growth and utility for over fifty years. Improvements in technology and electronic miniaturization have decreased the cost and size of ultrasound systems and made highly portable systems possible. In this section, the history and principles of diagnostic ultrasound are discussed.

16.2.1 Origins of Ultrasound Imaging

Though it has long been known that bats use sound for echolocation, the intentional use of ultrasound (sound with frequencies above our range of hearing) for this purpose began, surprisingly, with the sinking of the *Titanic* in 1913. L. F. Richardson, a British scientist, filed patents within months of the *Titanic* disaster for echolocation of icebergs (and other objects) using sound in either water or air. By the end of World War I, C. Chilowsky and P. Langevin in France invented practical implementations of echolocation with high-powered electronic transmitters and piezoelectric transducers for locating submarines and echo ranging. These principles of echo ranging were applied much later to electromagnetic waves to create RADAR (Radio Detection And Ranging). The circular sweep of a RADAR echo ranging line is displayed on PPI (plan position indicator) monitors, an early example of pulse-echo imaging. This type of display and technology was in turn adopted by underwater investigators to develop SONAR (SOUND Navigation And Ranging).

After experiencing these technologies during World War II, several doctors wanted to apply echolocation principles to the interior of the human body. Fortunately, a device—the supersonic reflectoscope—that was developed for finding defects in solid objects by ultrasound echolocation became available in addition to other surplus wartime equipment. This type of equipment sent out short pulses a few microseconds in length, repeated at longer intervals of a millisecond, as shown in Figure 16.1.

Short pulses were needed to determine the location of tissue boundaries. A typical setup is shown in Figure 16.2, along with a record of echoes displayed as a function of time. Here,

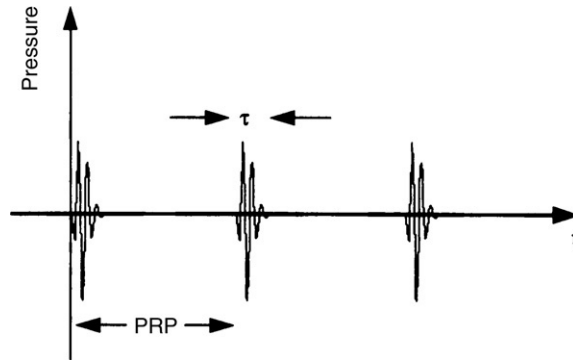


FIGURE 16.1 A plot of a series of transmitted acoustic pulses repeated at intervals called a pulse repetition period (PRP). Typically, the -3 dB width of a pulse is only a few microseconds in order to resolve different tissue interfaces, whereas the PRP is about a millisecond. For the purposes of illustration, the PRP has been compressed to enhance the presentation of pulses. The horizontal, or time, axis represents ambient pressure. Positive values on the vertical axis show compressional acoustic pressure, and negative values show rarefactional pressure.

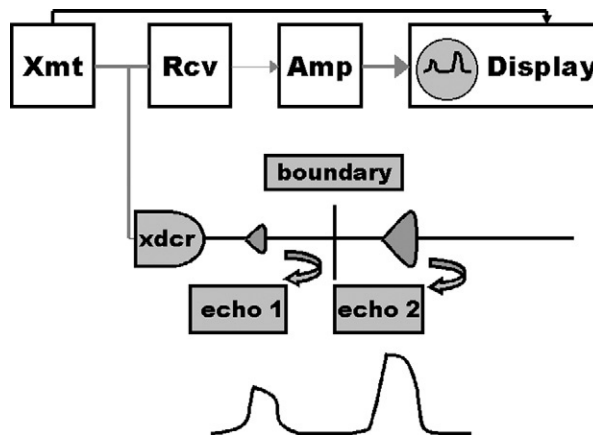


FIGURE 16.2 Basic echo ranging system consisting of a transmitter, a transducer, a receiver, an amplifier, and an oscilloscope display. Pulse echoes are shown below at delays corresponding to depths of reflecting objects above.

the delay, t , to each echo is the round-trip distance to the object, $2z$, divided by the speed of sound in the material, c , or $t = 2z/c$. The echo range instrument consisted of a piezoelectric transducer that converted the electrical pulses from the transmitter to acoustic pulses and reconverted received echoes from targets into electrical signals. These signals were then amplified and displayed as a time record on an oscilloscope. This type of display was known as an A-mode display, with A signifying amplitude.

In 1949, U.S. Naval doctor G. Ludwig reported his measurements of sound speed in parts of the body, and the results showed they had an average value of $c_0 = 1540$ m/s. More recent precise measurements showed that sound speed for most tissues varied by only a few percent, as listed in [Table 16.1](#). This important finding meant that the location of organs

TABLE 16.1 Acoustic Properties of Tissue

Material	C (m/s)	α (dB/MHz ^y -cm)	y	ρ (kg/m ³)	Z (MegaRayls)
Air	343			1.21	0.0004
Bone	3,360	3.54	0.9	1,789	6.00
Blood	1,550	0.14	1.21	1,039	1.61
Fat	1,450	0.6	1.0	952	1.38
Honey	2,030			1,420	2.89
Liver	1,570	0.45	1.05	1,051	1.65
Muscle	1,580	0.57	1.0	1,041	1.645
Water @ 20°C	1,482.3	2.17×10^{-3}	2.0	1,000	1.482

could be determined by the simple delay equation with a single value for sound speed, c_0 , which is still used today in modern imaging systems. In other words, the geometric accuracy of the placement of organs in an ultrasound image largely depends on the uniformity of the sound speed in the field of view. Ludwig also measured the characteristic acoustic impedance of tissues, $Z = \rho c$, in which ρ and c represent the density and speed of sound of each tissue, respectively. He found that at the boundary of two different tissues, the reflection factor was related to the impedances of the individual tissues, Z_1 and Z_2 :

$$RF = \frac{Z_2 - Z_1}{Z_2 + Z_1} \quad (16.6a)$$

Independently, Dr. D. Howry, another U.S. doctor, found that because the reflection factors were small, ultrasound penetrated through multiple layers of soft tissue with ease (except for regions with gas or bone). In 1956, he was able to make detailed anatomical maps of the body with sound and showed that they corresponded with known locations and sizes of organs and tissues. A graph of reflection factors in dB (decibels),

$$RF_{dB} = 20 \log_{10}(RF) \quad (16.6b)$$

all with reference to Z_1 for blood is shown in [Figure 16.3](#). These factors are different enough to provide adequate discrimination, an important factor in differentiating among tissues in imaging.

Dr. J. J. Wild, an English surgeon, and J. Reid, an electrical engineer (now professor emeritus) working in Minnesota with a surplus 15 MHz radar simulator in 1951, recognized the value of ultrasound for diagnosis and attempted to use it to detect cancer in the stomach. They also made calculations on pulse-echo waveforms to infer properties of healthy and diseased tissue and began a new field now called tissue characterization. In the process, Wild and Reid developed near real-time ultrasound imaging systems and ways of placing transducers (that transmit sound and receive pulse echoes and convert them to electrical signals) directly on the skin.

In the 1950s, a number of groups around the world became interested in the diagnostic possibilities of ultrasound. S. Satomura, Y. Nimura, and T. Yoshida in Japan detected blood

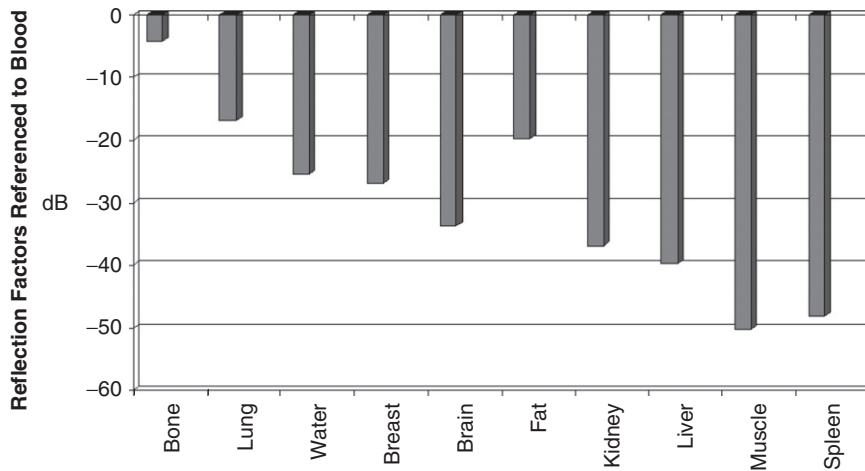


FIGURE 16.3 Amplitude reflection factor for tissues normalized to the impedance of blood and plotted on a decibel scale.

flow in the heart through Doppler-shifted motion, and I. Edler and C. H. Hertz in Sweden studied the motion of the heart and started echocardiography, the use of ultrasound to study the properties and dynamics of the heart.

Investigators around the world continued to make progress with the development of ultrasound imaging. Even though internal organs and the dynamics of heart motion could be detected with ultrasound, ultrasound remained a laboratory curiosity. Until the early 1960s, mothers and fetuses were imaged by x-rays. A 1956 report by Alice Stewart, an English epidemiologist, linked deaths from cancer in children to their mothers' exposure to x-rays during pregnancy. This tragic finding gave ultrasound imaging its first commercial opportunity to provide a safe alternative for fetal imaging.

During the early 1960s, several companies developed ultrasound imaging systems suitable for imaging fetuses and other internal organs. R. Soldner of Siemens designed the first real-time mechanical ultrasound imaging scanner in 1965 in Germany. Drs. I. McDonald and T. G. Brown developed the first commercially successful diagnostic ultrasound imaging system, the Disonograph, in 1968.

These investigators eventually preferred a pulse-echo method of ultrasound imaging with equipment similar to that shown in [Figure 16.4](#). The image is made up of a sequential arrangement of echo ranging lines, where each line would correspond to each pulse in a sequence, such as that depicted in [Figure 16.1](#). The diagram shows an oval-shaped object with a sound beam piercing it. The sound is transmitted, and received echoes corresponding to the front and back boundaries of the oval at that beam location are then displayed as white dots on a vertical echo line with time increasing in the downward direction on a monitor. Next, the transducer is moved to another location, and the process is repeated until all the lines have been sent. The resulting series of lines, geometrically arranged on the display to correspond to the actual positions of the transducer, result in an ultrasound image of the object. These early images were viewed either on long persistence cathode ray tubes or captured with

The two arguments in the exponents represent waves traveling along the positive z -axis and along the negative z -axis, respectively. For a constant frequency, for example, when the argument of the first term is equal to π , the term is real and has an amplitude of -1 . The next time the amplitude of the first term has this value is for an argument of 3π . For this situation, both t and z must increase; therefore, these arguments can be recognized as wavefronts that propagate forward with a delay equal to the distance divided by the sound speed, $t - z/c_0$.

If k is a wavenumber defined as

$$k = 2\pi f/c_0 = \omega/c_0 \quad (16.8)$$

and f is frequency, a sinusoidal wave can be interpreted as a function of propagation distance at a fixed time with a wavelength, $\lambda = 2\pi/k$, or as a function of time at a specific location with a period, $T = 2\pi/\omega$, as shown in [Figure 16.5](#).

The ratio of a traveling pressure wave, p , to the particle velocity, v , of the fluid is called the specific acoustic or characteristic impedance,

$$Z_L = p/v_L = \rho c_L \quad (16.9)$$

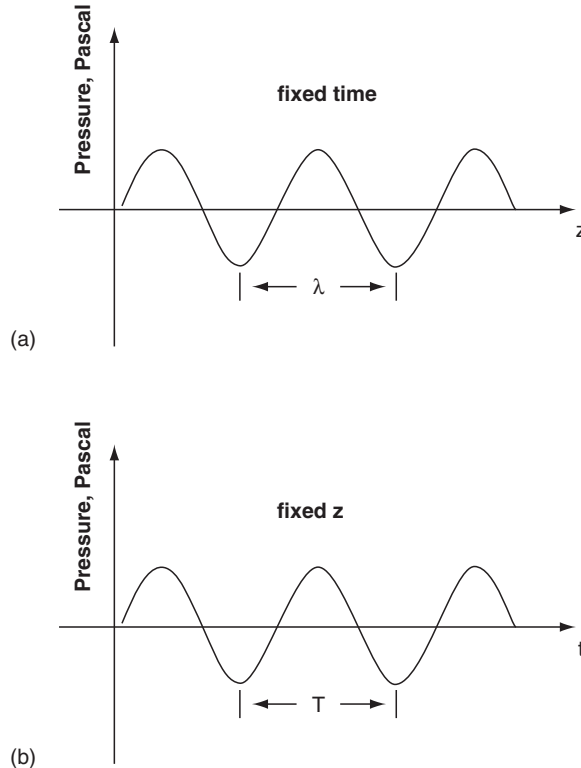


FIGURE 16.5 (a) Sinusoidal acoustic wave propagation as a function of space at a fixed time. (b) Sinusoidal acoustic wave propagation as a function of time at a fixed distance z ; pressure is the acoustic parameter plotted here. The distance and time between two troughs or peaks are defined as the wavelength, (λ), and period, (T), of the wave, respectively.

Note that Z_L is positive for forward traveling waves and negative for backward traveling waves. For fresh water at 20°C, $c_L = 1,481$ m/s, $Z_L = 1.48$ MegaRayls (10^6 kg/m² sec), and $\rho = 998$ kg/m³. The subscript L designates longitudinal waves, the type that is most important in imaging. In a longitudinal wave, the changes in wave amplitude are aligned along the direction of propagation with positive parts of sinusoidal waves, called compressional half cycles, and negative ones, called rarefactional half cycles, as depicted in Figure 16.5b.

The instantaneous intensity is

$$I_L = pv^* = pp^*/Z_L = vv^*Z_L \quad (16.10)$$

To determine the amplitude of a reflected wave, a solution similar to that of Eq. (16.7) can be applied. Consider the problem of a single frequency acoustic plane wave propagating in an ideal fluid medium a distance d to a boundary with a different medium, as shown in Figure 16.6. A plane wave is a sinusoidal-type wave with infinite extent in the lateral directions (x and y). For the example shown, the propagating medium has a wavenumber k_1 and an impedance Z_1 , whereas the second medium has impedance Z_2 and a wavenumber k_2 . As shown in Figure 16.6, the waves to the left of this second medium can be described by a combination of forward and backward traveling waves

$$p = p_0 \exp(i(\omega t - k_L z)) + RF p_0 \exp(i(\omega t + k_L z)) \quad (16.11)$$

which is a modified version of Eq. (16.7), $k_L = k_1$, and RF is a reflection factor for the amplitude of the negative going wave.

To determine the factor RF , it is useful to make analogies between acoustic variables and more well-known electrical parameters: pressure to voltage and particle velocity to electrical current. As shown in Figure 16.6, a source is situated at $z = d$, and the second medium is represented by a real load of impedance Z_2 located at $z = 0$, with a semi-infinite length. By analogy, the pressure at $z = 0$ is like a voltage drop across Z_2 , so from Eq. (16.11), drop out common $\exp(i\omega t)$ terms to obtain

$$p_2 = p_0 (1 + RF) \quad (16.12)$$

The particle velocity there is like the sum of currents flowing in opposite directions corresponding to the two wave components. From Eq. (16.9),

$$v_2 = (1 - RF)p_0/Z_1 \quad (16.13)$$

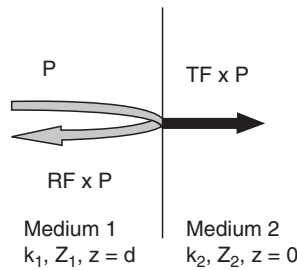


FIGURE 16.6 One-dimensional model of wave propagation at a boundary between media having impedances of Z_1 and Z_2 .

The impedance, Z_2 , can be found from

$$Z_2 = \frac{p_2}{v_2} = \frac{(1 + RF)Z_1}{1 - RF} \quad (16.14)$$

Finally, the right-hand side of Eq. (16.14) can be solved to obtain

$$RF = \frac{Z_2 - Z_1}{Z_2 + Z_1} \quad (16.15a)$$

A transmission factor, TF , can be determined from

$$TF = 1 + RF \quad (16.15b)$$

or

$$TF = \frac{2Z_2}{Z_1 + Z_2} \quad (16.15c)$$

EXAMPLE PROBLEM 16.2

Find the reflection and transmission factors for the case of a free, a perfectly matched, and a rigid boundary. What is the acoustic pressure transferred under these conditions? Assume water as medium 1.

Solution

For a free or air-type boundary or open-circuit condition, $Z_2 = 0$, so from Eq. (16.15a), there will be a 180° inversion of the incident wave, or $RF = -1$. Here, the reflected wave cancels the incident, so $TF = 0$. For a matched condition, $Z_2 = Z_1$, $RF = 0$ or no reflection, and $TF = 1$ for perfect amplitude transfer. For a rigid boundary, $Z_2 = \infty$, corresponding to a short-circuit condition or a stress-free boundary, and the incident wave will be reflected back, or $RF = +1$, without phase inversion. In this case, $TF = 2$.

Oblique Waves at a Liquid-Liquid Boundary

What happens when the incident wave is no longer normal to the boundary? This situation is depicted in Figure 16.7, in which a single-frequency longitudinal wave traveling in a liquid medium 1 is incident at an angle to a boundary with a different liquid medium 2 in the plane x - z . At the boundary, pressure and particle velocity are continuous. The tangential components of wavenumbers also must match, so along the boundary,

$$k_{1x} = k_1 \sin \theta_I = k_2 \sin \theta_T = k_1 \sin \theta_R \quad (16.16a)$$

where k_1 and k_2 are the wavenumbers for mediums 1 and 2, respectively. The reflected angle, θ_R , is equal to the incident angle, θ_I , and an acoustic Snell's law results,

$$\frac{\sin \theta_I}{\sin \theta_T} = \frac{c_1}{c_2} \quad (16.16b)$$

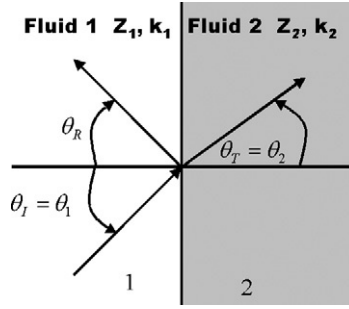


FIGURE 16.7 Oblique longitudinal waves at a liquid–liquid interface. The x -axis lies along the boundary, and the z -axis is normal to the boundary.

which can be used to find the angle θ_T . Equation (16.16a) enables the determination of θ_R . From the previous relations, the wavenumber components along z are

$$\text{incident } k_{Iz} = k_1 \cos \theta_I \quad (16.17a)$$

$$\text{reflected } k_{Rz} = k_1 \cos \theta_R \quad (16.17b)$$

$$\text{transmitted } k_{Tz} = k_2 \cos \theta_T \quad (16.17c)$$

which indicate that the effective impedances at different angles are

$$Z_{1\theta} = \frac{\rho_1 c_1}{\cos \theta_I} = \frac{Z_1}{\cos \theta_I} \quad (16.18a)$$

and

$$Z_{2\theta} = \frac{\rho_2 c_2}{\cos \theta_T} = \frac{Z_2}{\cos \theta_T} \quad (16.18b)$$

Here, the impedance is a function of angle that reduces to familiar values at normal incidence and otherwise becomes larger with angle. When the incident wave changes direction as it passes into medium 2, the bending of the wave is called refraction. For semi-infinite fluid media joined at a boundary, each medium is represented by its characteristic impedance given by Eqs. (16.18a) and (16.18b). Then, just before the boundary, the impedance looking toward medium 2 is given by Eq. (16.18b). The reflection coefficient there is given by Eq. (16.15a),

$$RF = \frac{Z_{2\theta} - Z_{1\theta}}{Z_{2\theta} + Z_{1\theta}} = \frac{Z_2 \cos \theta_I - Z_1 \cos \theta_T}{Z_2 \cos \theta_I + Z_1 \cos \theta_T} \quad (16.19a)$$

where the direction of the reflected wave is along θ_R , and the transmission factor along θ_T is

$$TF = \frac{2Z_{2\theta}}{Z_{1\theta} + Z_{2\theta}} = \frac{2Z_2 \cos \theta_I}{Z_2 \cos \theta_I + Z_1 \cos \theta_T} \quad (16.19b)$$

To solve these equations, θ_T is found first from Eq. (16.16b). This liquid–liquid interface is often used to model waves approximately at a tissue-to-tissue boundary.

EXAMPLE PROBLEM 16.3

For a wave incident at a water–honey interface, determine the reflection factor at 45° and at 50° . The sound speeds and impedances for water (medium 1) and honey (medium 2) are 1.48 km/s and 2.05 km/s and 1.48 MegaRayls and 2.89 MegaRayls, given in Table 16.1.

Solution

From Snell's law, Eq. (16.16b), $\theta_T = \arcsin[(2.05/1.48) \sin 45] = 78.4^\circ$. Then from Eq. (16.19a),

$$RF = \frac{2.89 \times \cos 45 - 1.48 \times \cos 78.4}{2.89 \times \cos 45 + 1.48 \times \cos 78.4} = 0.746$$

Before finding the result for 50° , it is worth finding the critical angle at which the incident wave is directed along the boundary. This angle, found by setting $\theta_T = 90^\circ$ in Snell's law, is known as the critical angle, which is $\theta_c = 46.22^\circ$ in this case. For an incident angle of 50° that is past the critical angle, the wave is just reflected and does not get transmitted, or $RF = 1$.

16.2.3 Transducer Basics

The essential part of an ultrasound system is a means to generate and receive acoustic waves. This function is performed by the transducer, which can convert electrical signals to acoustic pressure waves and vice versa. Inside the transducer is a piezoelectric crystal or ceramic that deforms when a voltage is applied and transmits acoustic waves. A reciprocal piezoelectric effect, in which electrical charge is created by the mechanical deformation of a crystal, allows the transducer to convert returning acoustic waves back to electrical signals. The piezoelectric effect was discovered by the Curie brothers in 1880.

A simple model is presented that describes the basic acoustic and electrical characteristics of a piezoelectric transducer. Consider a transducer to consist of a rectangular piece of piezoelectric material with electrodes on the sides, as shown in Figure 16.8. Each side has a cross-sectional area, A , with a top and bottom that are much longer ($>10X$) than the thickness, d . Because piezoelectric material is dielectric, it is essentially a capacitor with a clamped capacitance

$$C_0 = \varepsilon^S A/d \quad (16.20)$$

in which ε^S is a clamped dielectric constant under the condition of zero deformation. Because the crystal is a solid rather than a liquid, elastic waves are created internally. The elastic counterpart of pressure is stress, or force per unit area, represented by the symbol T . Another important elastic variable is strain, S , the relative change in length of the crystal divided by its original length. Both stress and strain vary with direction in a piezoelectric material, but for the single direction of wave propagation, it is possible to relate the stress to the strain as

$$T = C^D S - hD \quad (16.21)$$

in which h is a piezoelectric constant. This equation is known as a modified Hooke's law, in which the first term relates the stress to the strain and the second term relates stress to the

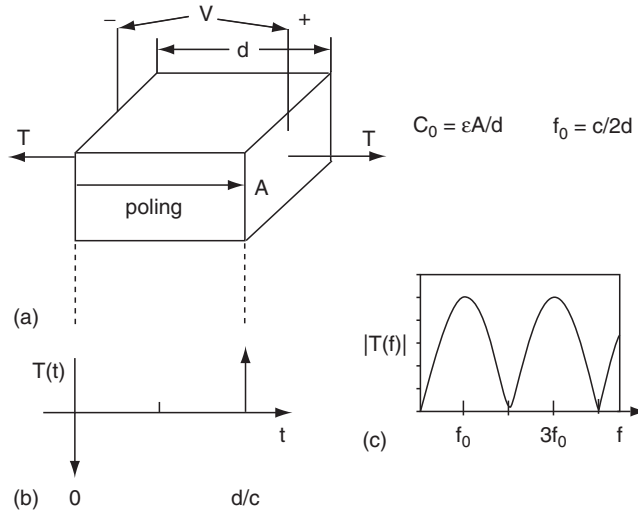


FIGURE 16.8 (a) Diagram for a piezoelectric crystal radiating into a medium matched to its impedance, (b) stress time response, and (c) stress frequency response.

applied electric field. The elastic stiffness constant, C^D , is obtained under a constant dielectric displacement, D , and if E is the electric field,

$$D = \epsilon^S E = \frac{\epsilon^S A V}{d A} = C_0 V / A \quad (16.22)$$

When a voltage impulse is applied across the electrodes, the piezoelectric effect creates impulsive forces at the sides of the transducer, given by

$$F(t) = T A = (h C_0 V / 2) [-\delta(t) + \delta(t - d/c)] \quad (16.23)$$

where the media above and below have the same acoustic impedance, Z_c , as the transducer; the speed of sound between the electrodes is given by $c = \sqrt{C^D / \rho}$, and δ represents an impulse (see Figure 16.8b).

Since it can create acoustic waves, the crystal could be regarded as a singing capacitor with its own unique voice or spectral characteristics and resonant frequency. To obtain the spectrum of this response, take the Fourier transform of Eq. (16.23),

$$F(f) = -i(h C_0 V) e^{\frac{-i \pi f d}{c}} \sin [\pi(2n + 1)f / 2f_0] \quad (16.24)$$

which has maxima at odd harmonics (note $n = 0, 1, 2, 3, \dots$) of the fundamental resonance $f_0 = c/2d$, as shown in Figure 16.8c.

Transducer Electrical Impedance

Because of the forces generated at the sides of the transducer, the electrical impedance looking through the voltage terminals is affected. Across the wires connected to the transducer (Figure 16.8a), a radiation impedance, Z_A , is seen in addition to the capacitive reactance, so the overall electrical impedance is

$$Z_T = Z_A - i(1/\omega C_0) = R_A(f) + i[X_A(f) - 1/\omega C_0] \quad (16.25)$$

From the transducer electrical equivalent circuit in Figure 16.9a, Z_A is radiation impedance of which R_A and Z_A are its real and imaginary parts. $R_A(f)$ can be found from the total real electrical power, W_E , flowing into the transducer for an applied voltage V , and current I

$$W_E = II^* R_A / 2 = |I|^2 R_A / 2 \quad (16.26a)$$

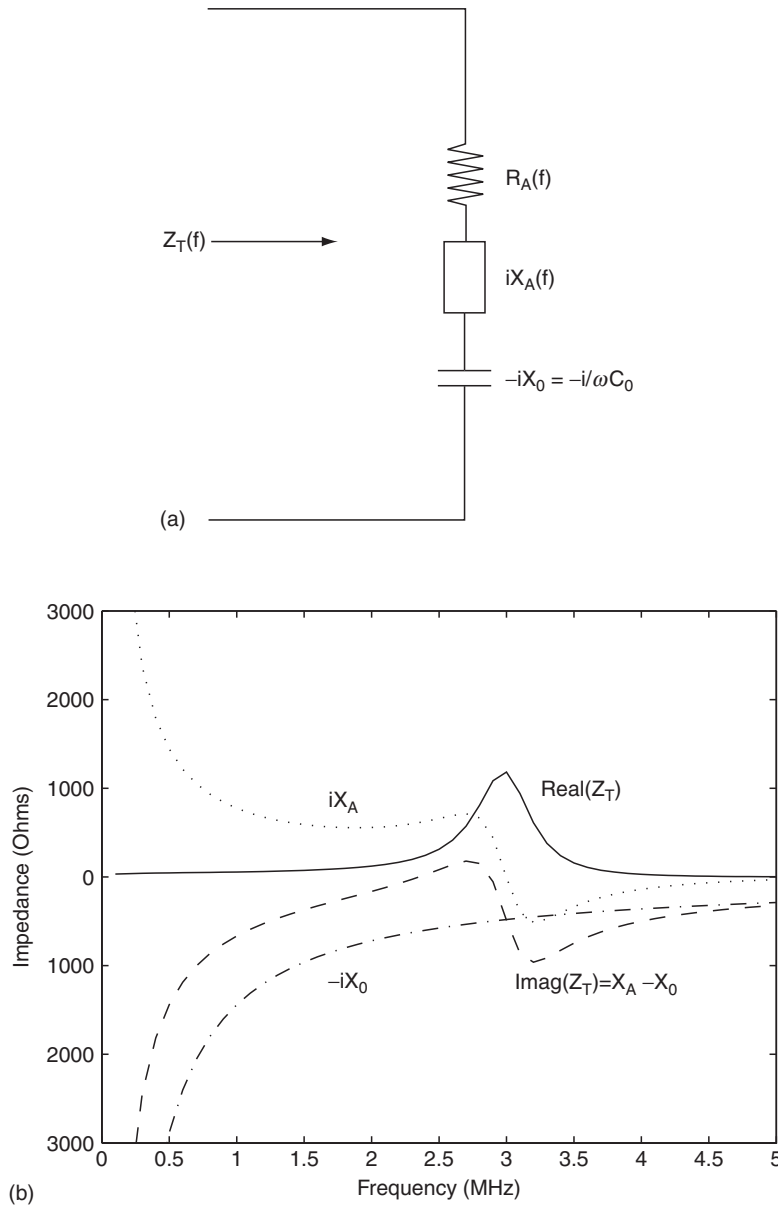


FIGURE 16.9 (a) Transducer equivalent circuit and (b) transducer impedance as a function of frequency.

where current is $I = i\omega Q = i\omega C_0 V$ and Q is charge. The total power radiated from both sides of the transducer into a surrounding medium of a modified specific acoustic impedance (including an area factor), $Z_C = \rho c A$, equal to that of the crystal, is

$$W_A = ATT^*/(2Z_C/A) = A^2|F(f)/A|^2/2Z_C = |hC_0 V \sin(\pi f/2f_0)|^2/2Z_C. \quad (16.26b)$$

Setting the powers of Eqs. (16.26a) and (16.26b) equal leads to a solution for R_A

$$R_A(f) = R_{AC} \sin^2 c^2(f = 2f_0) \quad (16.27a)$$

where $\sin c(x) = \sin(\pi x)/(\pi x)$ and

$$R_{AC} = \frac{k_T^2}{4f_0 C_0} = \frac{d^2 k_T^2}{2A \epsilon^S} \quad (16.27b)$$

in which the electroacoustic coupling constant is k_T , and $k_T = h/\sqrt{C^D/\epsilon^S}$. Note that R_{AC} is inversely proportional to the capacitance and area of the transducer and directly dependent on the square of the thickness, d . Also, note that at resonance,

$$R_A(f_0) = \frac{k_T^2}{\pi^2 f_0 C_0} \quad (16.27c)$$

Network theory requires that the imaginary part of an impedance be related to the real part through a Hilbert transform, so the radiation reactance can be found as

$$X_A(f) = \Im_{Hi}[R_A(f)] = R_{AC} \frac{[\sin(\pi f/f_0) - \pi f/f_0]}{2(\pi f/2f_0)^2} \quad (16.28)$$

The transducer impedance is plotted as a function of frequency in Figure 16.9b. Here R_A is maximum at the resonant frequency f_0 and X_A is zero.

This simple model describes the essential characteristics of a piezoelectric transducer. The electrical impedance has a maximum of real radiation resistance at the resonant frequency. The force spectrum is also peaked at the resonant frequency and has a certain shape.

EXAMPLE PROBLEM 16.4

Find the transducer impedance at resonance for a square transducer 2.5 mm on a side for a resonant frequency of 3 MHz for the ceramic PZT5A with $\epsilon^s/\epsilon_0 = 830$, $c = 4.35$ km/s, $k_T = 0.49$, and $\epsilon_0 = 8.85$ pF/m.

Solution

First find the thickness needed to achieve a resonant frequency of 3 MHz from $f_0 = c/2d$, or $d = c/2f_0 = 4.35 \text{ mm}/\mu\text{s}/2 \times 3 \text{ MHz} = 0.725 \text{ mm}$. Then the capacitance is

$$C_0 = \frac{830 \times 8.85 \times 10^{-12} \text{ F/m} \times (2.5 \times 10^{-3} \text{ m})^2}{7.25 \times 10^{-4} \text{ m}} = 63.3 \text{ pF}$$

Find R_A from Eq. (16.27c):

$$R_A = \frac{0.49^2}{\pi^2 \times 3 \times 10^6 \text{ Hz} \times 63.3 \times 10^{-12} \text{ F}} = 128.2 \text{ ohms}$$

Note that the units in the denominator are $\text{Hz} \cdot \text{F} = \text{amps/volt} = \text{ohm}^{-1}$. Then, since at resonance $x_A = 0$, from Eq. (16.25),

$$Z_T = 128 - i/(2 \times \pi \times 3 \times 10^6 \text{ Hz} \times 63.3 \times 10^{-12} \text{ F}) = 128 - i838 \text{ ohms}$$

Transducer Frequency Response

Transducer design is concerned with altering the shape of the spectrum to achieve a desired bandwidth and a short, well-behaved pulse shape, or impulse response. Another design goal is to improve the electroacoustic efficiency of the transducer. One measure of this efficiency is transducer loss, the ratio of time average acoustic power reaching the desired medium, usually tissue, W_R , divided by the maximum electrical power available from an electrical source, W_g ,

$$TL(f) = \frac{W_R}{W_g} \quad (16.29a)$$

and defined in dB as

$$TL_{\text{dB}}(f) = 10 \log_{10} TL(f) \quad (16.29b)$$

The transducer loss can be broken down into an electrical loss factor, $EL(f)$, and an acoustic loss factor, $AL(f)$:

$$TL(f) = EL(f)AL(f) \quad (16.30)$$

The problem of optimizing the transfer of electrical power into the radiation resistance is that of maximizing $EL(f)$ over a desired bandwidth. Figure 16.10 shows the relevant parameters involved. The transducer electrical impedance is connected through a tuning inductor to a voltage source with impedance R_g . An expression for electrical loss for this situation is

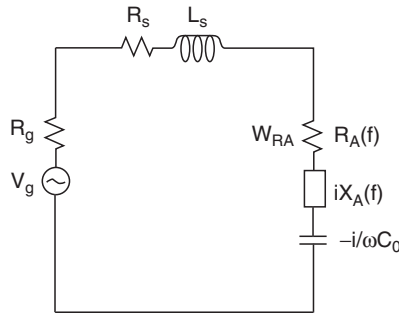


FIGURE 16.10 Electrical voltage source with tuning inductor connected to transducer equivalent circuit.

$$EL(f) = \frac{4R_A(f)R_g}{(R_A(f) + R_g + R_s)^2 + \left(X_A(f) - \frac{1}{\omega C_0} + \omega L_s\right)^2} \quad (16.31a)$$

If the capacitance is tuned out by a series inductor, $L_s = 1/(\omega_0^2 C_0)$ and $R_s = 0$, then at resonance,

$$EL(f_0) = \frac{4R_A(f_0)R_g}{[R_A(f_0) + R_g]^2} \quad (16.31b)$$

Notice that if $R_A = R_g$, and $R_s \ll R_g$, then $EL(f_0) \sim 1$.

The determination of acoustic loss is a more complicated function of frequency, but it is straightforward to determine its value at resonance. In the simple transducer model introduced in [Section 16.2.3](#), a simplifying assumption was made that the acoustic loading on both sides of the piezoelectric crystal was the same acoustic impedance as that of the crystal; however, this is not the case in general, as illustrated in [Figure 16.11](#). Note the arrangement in this figure is rotated 90° from that in [Figure 16.8](#). On the top of this figure, the piezoelectric is loaded by a backing material and below the lens, by water or tissue. The bottom of the crystal shown here is usually regarded as the “business end” of the transducer, where the forward waves propagate along the positive z-axis that is directed downward in [Figure 16.11](#). Waves in the backward direction are suppressed or absorbed by a backing material that aids in broadening the spectrum of the transducer. By the left-right convention of [Figure 16.8](#), if the acoustic impedance looking out of the crystal to the left is Z_L , then that to the right along the positive z-axis is Z_R . In the case shown on the left

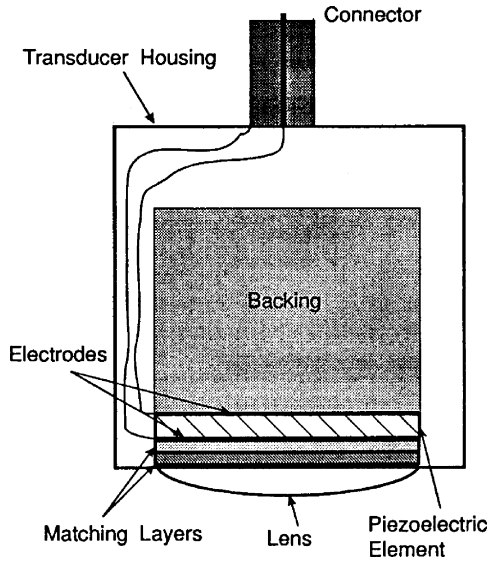


FIGURE 16.11 Construction of a single-crystal mechanical transducer. Forward propagation is directed downward.

of the figure, $Z_L = Z_B$ (backing impedance) and $Z_R = Z_W$ (impedance of water). The acoustic loss for this case at resonance can be found from (note all these impedances include the area factor A)

$$AL(f_0) = Z_R / (Z_L + Z_R) = Z_W / (Z_B + Z_W) \quad (16.32)$$

The physical meaning of this equation is that the electrical power reaching the radiation resistance is converted into acoustical power radiating from the two electroded faces of the piezoelectric; the proportion of power in the forward (right) direction is represented by the ratio in Eq. (16.32).

Construction of a single crystal transducer is shown in Figure 16.11. The key parts are the backing, the piezoelectric crystal coated with thin electrodes for electrical contact, matching layers, and a lens material, with an acoustic impedance close to water, for focusing (discussed in more detail in Section 16.2.6). Matching layers will be discussed shortly; in practice, more than one matching layer is used to broaden the bandwidth of the transducer.

In the first simple model, the crystal was loaded by acoustic impedances equal to that of the crystal, or $Z_C = Z_L = Z_R$ so that $AL(f_0) = 0.5$, as expected. Another example is that in which the left side is loaded by air or $Z_L = 0A$ MRayls, and the right by water, $Z_R = 1.5A$ MRayls. In this case, $AL(f_0) = 1.0$ but at the expense of extremely narrow bandwidth and a correspondingly long pulse. One case of interest is where the backing material is matched to that of the crystal so that $Z_L = Z_C = 30A$ MRayls and $Z_R = 1.5A$ MRayls, and $AL(f_0) = 0.048$, an inefficient transfer.

To improve the forward transfer efficiency, as described by the acoustic loss factor, matching layers are employed. At the resonant frequency, a matching layer is designed to be a quarter of a wavelength thick and to be the mean value of the two impedances to be matched, or

$$Z_{ml} = \sqrt{Z_1 Z_2} \quad (16.33)$$

EXAMPLE PROBLEM 16.5

Match a crystal of impedance $Z_c = 30A$ MRayls to water, $Z_w = 1.5A$ MRayls.

Solution

From Eq. (16.33), the matching layer impedance is

$$Z_{ml} = \sqrt{Z_W Z_C} = \sqrt{1.5A \text{ MRayls} \times 30A \text{ MRayls}} = 6.7A \text{ MRayls}$$

The acoustic input impedance at resonance is

$$Z_1 = Z_{ml}^2 / Z_2$$

therefore, the impedance looking to the right is

$$Z_R = Z_{ml}^2 / Z_W = (6.7A)^2 / 1.5A = 30A \text{ MRayls}$$

leading to $A(f_0) = 30 / (30 + 30) = 0.5$ for a water load with an intervening matching layer or an improvement of over 10 dB.

Continued

The effect of adding a matching layer can be included in a more generalized equation for radiation resistance at resonance by adding the loading from both sides,

$$R_A(f_0) = \frac{2k_T^2}{\pi^2 f_0 C_0} \left(\frac{Z_c}{Z_L + Z_R} \right) \quad (16.34)$$

The acoustical and electrical losses can now be combined to estimate the overall transducer loss. To do this, a simplification is made for the purposes of illustration that the acoustical loss is constant over the transducer bandwidth. The actual losses can be computed accurately by a more complete equivalent circuit model. From Eqs. (16.30) and (16.31a),

$$TL(f) \approx \left[\frac{4R_A(f)R_g}{(R_A(f) + R_g + R_s)^2 + (X_A(f) - \frac{1}{\omega C_0} + \omega L_s)^2} \right] \left[\frac{Z_R}{Z_R + Z_L} \right] \quad (16.35)$$

EXAMPLE PROBLEM 16.6

Find the transducer loss at resonance for the transducer described in Example Problem 16.4 under the following two conditions for a source resistance $R_g = 50\Omega$ (ohms): (1) No tuning, $Z_L = Z_B = 6A$ MRayls and $Z_R = Z_W = 1.5A$ MRayls. (2) Add a tuning inductor and a matching layer.

Solution

(1) Here, $R_A = 128$ ohms, $\frac{1}{\omega C_0} = 838$ ohms,

$$\begin{aligned} TL(f_0) &= \frac{4 \times 128 \text{ ohms} \times 50 \text{ ohms}}{(128 \text{ ohms} + 50 \text{ ohms})^2 + (838 \text{ ohms})^2} \times \frac{1.5A}{6A + 1.5A} \\ &= 6.98 \times 10^{-3} \text{ or } 10 \log_{10}(TL) \\ &= -21.6 \text{ dB} \end{aligned}$$

(2) R_A is determined from Eq. (16.34) and Example Problem 16.4, ohms. For tuning, find $L_s = 1/(\omega_0^2 C_0) = 838/(2\pi \times 3e6) = 44.5 \mu H$. Then,

$$\begin{aligned} TL(f_0) &= \frac{4 \times 128 \text{ ohms} \times 50 \text{ ohms}}{(128 \text{ ohms} + 50 \text{ ohms})^2 + (838 \text{ ohms} - 838 \text{ ohms})^2} \times \frac{30A}{30A + 1.5A} \\ &= .673 \times \text{ or } 10 \log_{10}(TL) \\ &= -1.72 \text{ dB} \end{aligned}$$

One way of describing the difference in shapes as a figure of merit is that a bandwidth is stated in dB. For example, a -6 dB bandwidth is defined relative to the peak spectral value. A center frequency is defined through the upper and lower -6 dB frequencies as

$$f_c = (f_{high} - f_{low})/2$$

An example of a -6 dB bandwidth with its associated frequencies is shown in Figure 16.12. Also included in this figure are similar widths for the pulse envelope (pulse-widths) in dB levels.

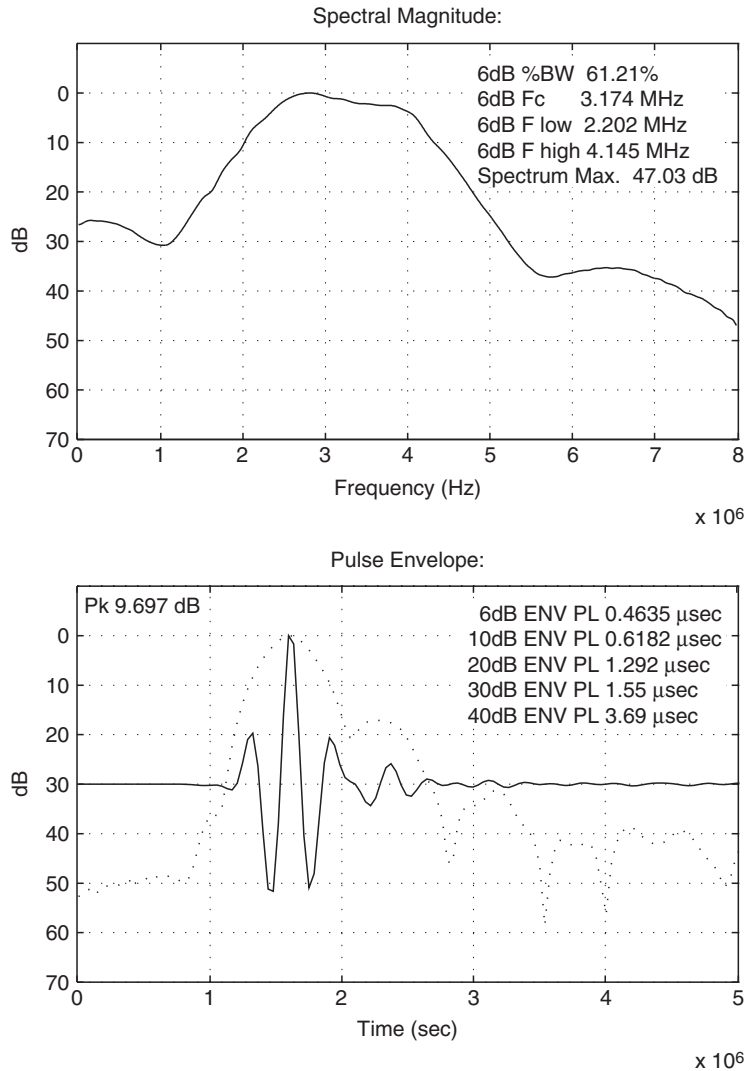


FIGURE 16.12 (Top) Transducer response spectral magnitude and -6 dB bandwidth dB. (Bottom) Transducer impulse response and its envelope measured in pulse-widths in dB.

Transducer Types and Arrays

Most imaging systems use arrays rather than single-crystal transducers. A one-dimensional array is an in-line arrangement of transducers called elements that are addressable individually or in small groups. The elements are spaced at regular intervals, typically one-half to two wavelengths apart in water ([Figure 16.13](#)). The key advantages of arrays are that they can be rapidly focused and steered electronically or electrically switched, whereas a strictly mechanical single transducer has a fixed focal length and can only be

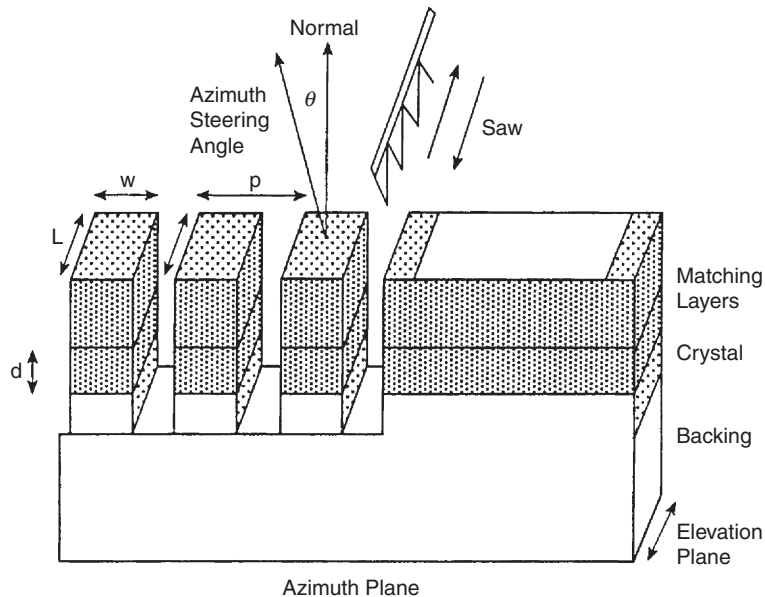


FIGURE 16.13 Construction of a one-dimensional array with a saw dicing up a multilayer sandwich structure into individual elements. Here, the propagation direction is along the normal axis, pointing upward.

steered or translated mechanically. Each element, in terms of basic design, is treated as an individual transducer. Arrays and focusing will be discussed in more detail in [Section 16.2.6](#) on diffraction.

The two most common types of arrays are the linear array and the phased array. The linear array forms an image by translating the active aperture (a certain number of elements) one element at a time along the length of the array, as shown in [Figure 16.14a](#). At each position of the active aperture, an acoustic line is created (i.e., a pulse-echo time record of a selected length or scan depth). A total number of lines, N , is formed in this

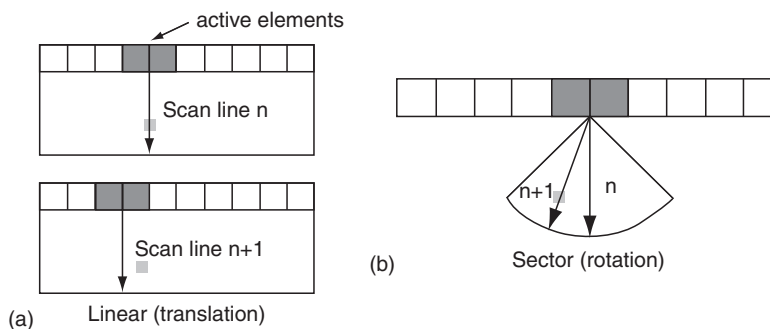


FIGURE 16.14 The time sequencing used for image formation for (a) linear array format and (b) sector array format.

way. In a phased array, the center of the active aperture is always the same, and the scanning of acoustic lines is accomplished through electronic angular steering. Each line is steered by a small incremental angle from the previous one, as shown in Figure 16.14b. When N lines have been received, these lines form the basis for an image frame. Examples of the image formats formed by these two array types can be seen in the B-mode images of Figures 16.15 and 16.16. A variant of the linear array is the curved linear array, which operates like a linear array but on a curved convex surface rather than on a flat surface. An example of an image from a curved linear array can be seen in Figure 16.17.

EXAMPLE PROBLEM 16.7

For the example shown in Figure 16.14a, determine the frame rate for a scan depth of $s_d = 150$ mm, 100 lines per frame, and $c_0 = 1.5$ mm/ μ s.

Solution

The round-trip time for one line is $2s_d/c_0 = 200$ μ s. The time for a full frame is N lines/frame or, in this case, 100 lines/frame $\times 200$ μ s/line = 20 ms/frame or 50 frames per second.

Transducer arrays come in a variety of sizes, shapes, and center frequencies to suit different clinical applications, as shown in Figure 16.18. Access to the body is made externally through many possible “acoustic windows,” where a transducer makes contact by coupling



FIGURE 16.15 B-mode image of lymph nodes in the breast at 12 MHz, an example of a linear array format. Courtesy of Philips Medical Systems.

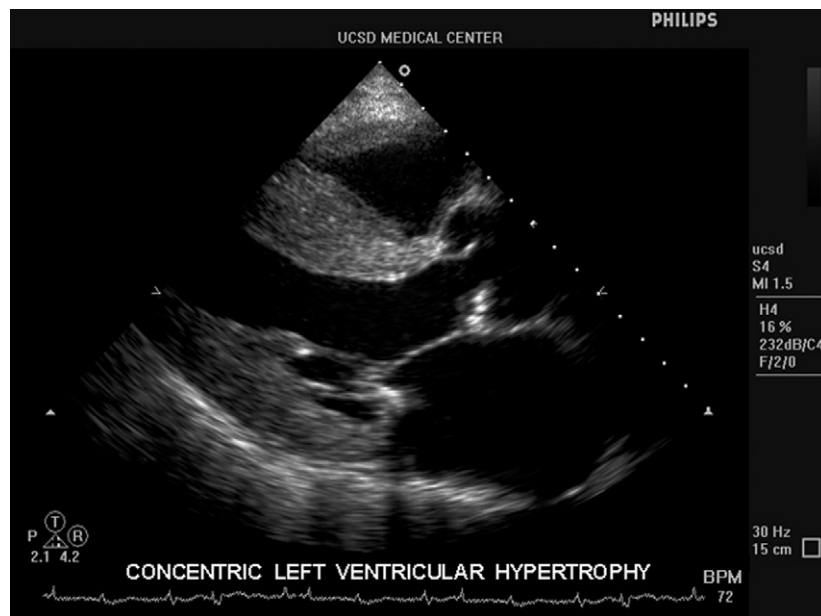


FIGURE 16.16 B-mode image of the heart at 4 MHz, an example of a sector array format. *Courtesy of Philips Medical Systems.*

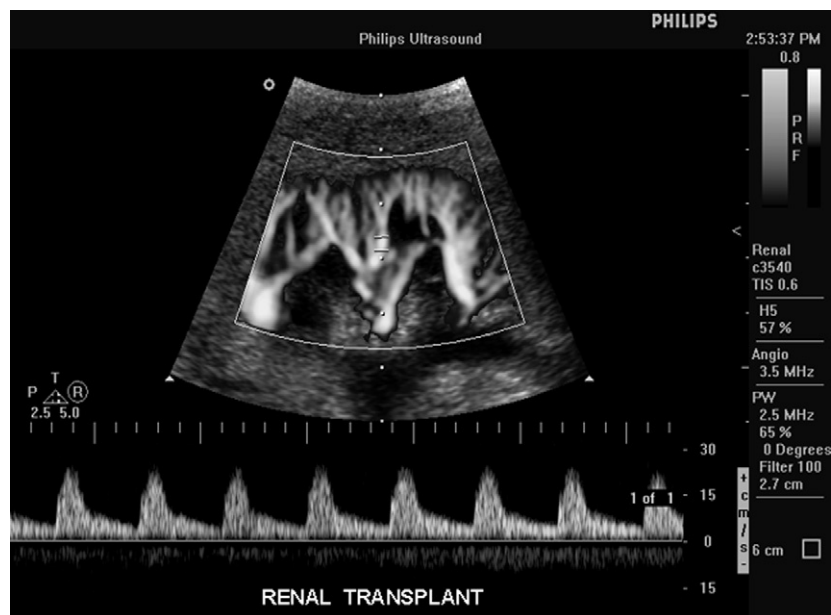


FIGURE 16.17 (Top) Power Doppler image of kidney with pulsed Doppler line down the center and Doppler gate in center of line. (Below) Corresponding pulsed wave Doppler spectrum. Image from a curved linear array. *Courtesy of Philips Medical Systems.*

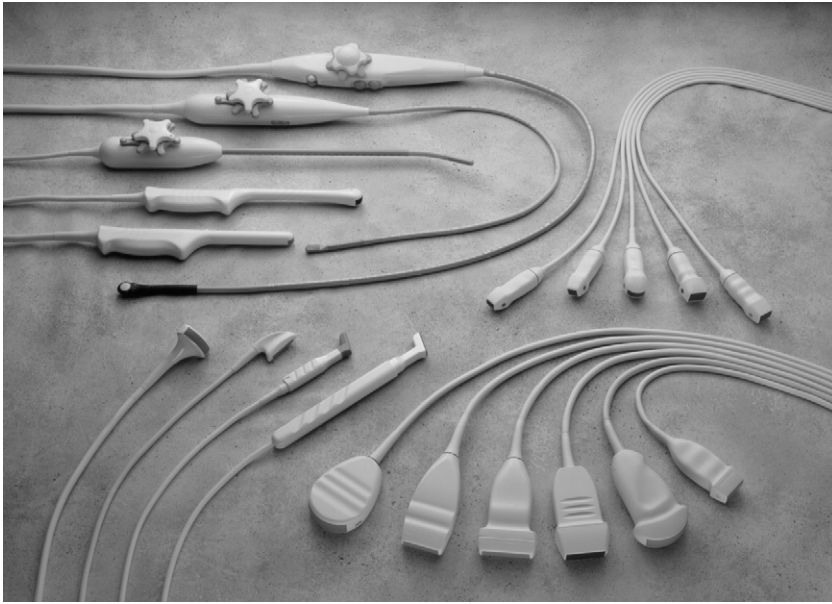


FIGURE 16.18 Transducers available on a modern imaging system are designed for a wide variety of clinical applications. Transducer groups: bottom right: linear and curved linear arrays; top right: phased arrays; left side: specialty probes including intraoperative, transesophageal, and transvaginal arrays. *Courtesy of Philips Medical Systems.*

to the body with a water-based gel. Except for regions containing bones, air, or gas, which are opaque to imaging transducers, even small windows can be enough to visualize large interior regions. The limitation of accessibility to viewing certain organs clearly is offset by specialized probes such as transesophageal (down the throat) and intracardiac (inside the heart) transducers that image from within the body.

16.2.4 Scattering

Interference of waves within the transducer plays an important role in the transduction process. The crystal resonates when its thickness is half a wavelength, and the matching layer is designed to be a quarter of a wavelength thick at resonance. The size of an object relative to a wavelength is also a useful way of looking at acoustic scattering from objects. Since ultrasound imaging is based on pulse-echoes returning from organs, it is necessary to determine how the reflected signals are affected by the dimensions and shape of an object relative to the insonifying wavelength.

Scattering falls within three ranges of effects: specular, diffractive, and diffusive ([Figure 16.19](#)). Specular scattering is already familiar. When the dimensions of an object are much greater than a wavelength, the reflected sound returns at the reflected angle equal to the incident angle relative to the surface, as described in [Section 16.2.2](#) on refraction. In this case, the reflected amplitude is determined by the reflection

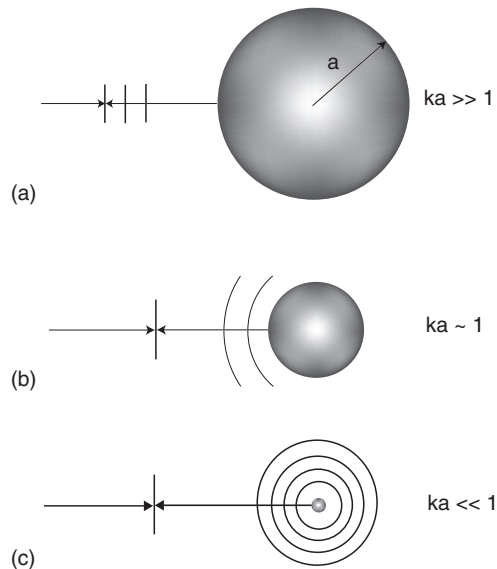


FIGURE 16.19 (a) Specular scattering from an object much greater than a wavelength. (b) Diffractive scattering from an object on the order of wavelengths. (c) Diffusive scattering from an object much smaller than a wavelength.

factor appropriate for the angle of incidence. At the other extreme, when an object is much smaller than a wavelength, its reflections are diffusive. Here, the object is so small relative to a wavelength that its features no longer contribute to the reflected wave. If the object is a sphere, then the reflected pressure is proportional to the frequency squared, inversely with the radius cubed and a term related to the differences in elastic constants and densities between the sphere and the surrounding medium.

The intermediate range between these two extremes, diffractive scattering, occurs when the dimensions of the object are on the order of wavelengths. If the surface of the object is divided into infinitesimal points and lines are drawn from these points to an observation point, then the differences in path lengths along these lines can be significant in terms of wavelengths. Contributions from these points could cause constructive and destructive interference effects at the observation point because of phase differences along the paths. Depending on the shape of the object and its orientation and distance to an observation point, complicated scattering patterns can result. Even for simply shaped objects, such as spheres or cylinders, the scattering pattern or directivity of these objects is highly frequency dependent as the object shape and dimensions change relative to a wavelength.

Human optical vision depends mainly on specular reflections (objects much greater than wavelengths of light). An acoustic image is formed from pulse-echoes along acoustic lines from an observation point to parts of the object. Unlike optics, the acoustic appearance of an object can change both with the orientation of the observer relative to the object and with the insonifying frequency.

16.2.5 Absorption

When waves propagate in real media, losses are involved. Just as forces encounter friction, pressure, and stress, waves lose energy to the medium of propagation and result in weak local heating. These small losses are called attenuation and can be described by an exponential law with distance. For a single frequency, f_c , plane wave, a multiplicative amplitude loss term can be added:

$$A(z, t) = A_0 \exp(i(\omega_c t - kz)) \exp(-\alpha z) \quad (16.36)$$

The attenuation factor, α , is usually expressed in terms of nepers/cm in this form. Another frequently used measure of amplitude is the deciBel (dB), which is most often given as the ratio of two amplitudes, A and A_0 on a logarithmic scale

$$\text{Ratio(dB)} = 20 \log_{10}(A/A_0) \quad (16.37)$$

or in those cases where intensity is simply proportional to amplitude squared ($I_0 \propto A_0^2$),

$$\text{Ratio(dB)} = 10 \log_{10}(I/I_0) = 10 \log_{10}(A/A_0)^2 \quad (16.38)$$

Most often, α , is given in dB/cm:

$$\alpha_{dB} = 1/z \{20 \times \log_{10}[\exp(-\alpha_{\text{nepers}} z)]\} = 8.6886 (\alpha_{\text{nepers}}) \quad (16.39)$$

Data indicate that the absorption is a function of frequency (see [Table 16.1](#)). Many of these losses obey a frequency power law defined as

$$\alpha(f) = \alpha_0 |f|^y \quad (16.40)$$

in which y is a power law exponent. The pressure amplitude can be written to first order as a function of frequency

$$A(z, f) = A_0 \exp(-i2\pi f z/c) \exp[-\alpha_0 |f|^y z] \quad (16.41)$$

where the first factor describes the propagation delay to z . The actual loss per wavenumber is very small, or $\alpha/k \ll 1$. Even though the loss per wavelength is small, absorption has a strong cumulative effect over many wavelengths. Absorption for a round-trip echo path usually determines the allowable tissue penetration for imaging.

EXAMPLE PROBLEM 16.8

Determine the absorption loss for 10 cm of propagation in muscle for a frequency of 5 MHz.

Solution

From [Table 16.1](#), $\alpha_0 = 0.57$ dB/cm-MHz. Method 1: Convert the absorption coefficient to nepers from [Eq. \(16.39\)](#), α (nepers/MHz-cm) = $0.57/8.6886 = 0.0656$. Use this value in [Eq. \(16.41\)](#) to obtain $A/A_0 = \exp(-0.0656 \text{ nepers/MHz-cm} \times 5 \text{ MHz} \times 10 \text{ cm}) = 3.76 \times 10^{-2}$. In dB terms, $20 \log_{10}(A/A_0) = -28.5$ dB. Method 2: If the linear answer is not needed, the answer in dB can be obtained directly by using the absorption coefficient in dB as $\alpha_0 f z = -0.57 \text{ dB/MHz-cm} \times 5 \text{ MHz} \times 10 \text{ cm} = -28.5$ dB.

16.2.6 Diffraction

Waves transmitted by a transducer are not plain but form a complicated pattern. The formation of these patterns, as shown in Figure 16.20, is caused by the radiation of sound waves from different locations on the aperture (transducer face) and the mutual interference of these radiated waves. This phenomenon, also called diffraction, is a consequence of the aperture dimensions that are on the order of wavelengths.

The two most common aperture shapes are the circle and rectangle, as shown in Figure 16.21. A slice of the three-dimensional beam in a plane is what is usually depicted in graphs. For the circle, because of symmetry, any plane through the beam axis (here the z -axis) will be identical. For the rectangular aperture, the beam formation differs in all planes through the beam axis, and the most important planes for imaging are the x - z and y - z planes. The beam amplitude described by Figure 16.20 corresponds to an x - z plane from a rectangular aperture.

Beams have recognizable landmarks. A method borrowed from maps is a contour plot of the acoustic pressure magnitude, often depicted in dB relative to maximum amplitude at each depth. Of particular interest is the -6 dB contour. A cross section of the beam, perpendicular to the beam axis, is called a beam plot. The width between points of this -6 dB

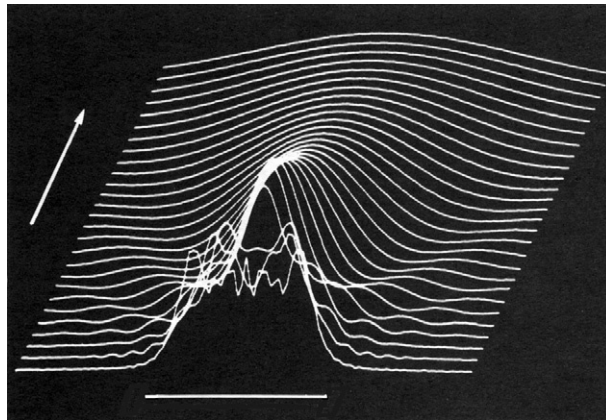


FIGURE 16.20 Diffracted field of a 40-wavelength-wide line aperture along the x -axis. The vertical axis intensity and beam profiles are shown at intervals of about 70 wavelengths along the beam axis that is compressed relative to the lateral dimension (1,920 wavelengths are shown along the z -axis).

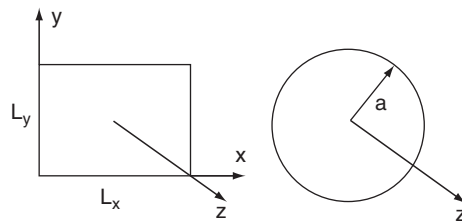


FIGURE 16.21 (Left) Circular aperture of radius a . (Right) Rectangular aperture with lengths of L_x parallel to the x -axis and L_y parallel to the y -axis. The z -axis is perpendicular to the x - y plane of the aperture.

contour on a beam plot is called the full-width-half-maximum (FWHM). A curious outcome of the radiation from these apertures is that there is a region in which the beam narrows. The depth where the last axial peak occurs is called the transition distance or natural focal length, F_N . This transition depth demarcates two regions, one with peaks and valleys, called the near field, and one with a beam with a single peak diminishing in amplitude width and broadening with distance, called the far field, as shown in [Figure 16.20](#). The transition depth for a circular aperture of radius a is

$$z_t = a^2/\lambda \quad (16.42a)$$

For a rectangular aperture, the transition distance for an aperture L_x in the x - z plane is

$$z_t \approx L_x^2/(\pi\lambda) \quad (16.42b)$$

The natural focal length is the distance to the last axial peak and is approximately the transition distance.

The far-field beam pattern for a rectangular aperture is the Fourier transform of the amplitude across the aperture. In the case of uniform illumination

$$A(x_0, y_0, 0) = \prod(x_0/L_x) \prod(y_0/L_y) \quad (16.43a)$$

where

$$\prod(x/L) = \begin{cases} 0 & |x| > L/2 \\ 1/2 & |x| = L/2 \\ 1 & |x| < L/2 \end{cases} \quad (16.43b)$$

the far-field pattern in the x - z plane is a sinc function

$$p(x, z, \omega) = \frac{L_x \sqrt{p_0}}{\sqrt{\lambda z}} e^{i\pi/4} \frac{\sin(\pi x x/\lambda z)}{(\pi L_x x/\lambda z)} = \frac{L_x \sqrt{p_0}}{\sqrt{\lambda z}} e^{i\pi/4} \text{sinc}\left(\frac{L_x x}{\lambda z}\right) \quad (16.44a)$$

A plot of this pattern is shown in [Figure 16.22](#).

In the case of a uniform amplitude u_0 on a circular aperture, the far-field pattern is the two-dimensional Fourier transform of the circularly symmetric aperture function

$$p(\bar{\rho}, z, \lambda) \approx \frac{ip_0 \pi a^2 2J_1(2\pi \bar{\rho} a/(\lambda z))}{2\pi \bar{\rho} a/(\lambda z)} = ip_0 \left(\frac{\pi a^2}{\lambda z}\right) jinc\left(\frac{\bar{\rho} a}{\lambda z}\right) \quad (16.44b)$$

where J_1 is the Bessel function of the first kind, $jinc(x) = 2J_1(2\pi x)/(2\pi x)$, and $\bar{\rho}$ is the radial distance to an observation point at $(\bar{\rho}, z)$. A plot of this pattern is shown in [Figure 16.22](#). Note that the shapes of the far-field patterns are maintained with distance as their amplitudes fall and beams broaden with distance.

From these far-field patterns, it is easy to determine the FWHM beam widths. For the rectangular aperture in the x - z or y - z plane

$$\text{FWHM} = 1.206\lambda z/L \quad (16.45a)$$

where L is the appropriate aperture for that plane. Similarly, for a circular aperture

$$\text{FWHM} = 0.7047\lambda z/a \quad (16.45b)$$

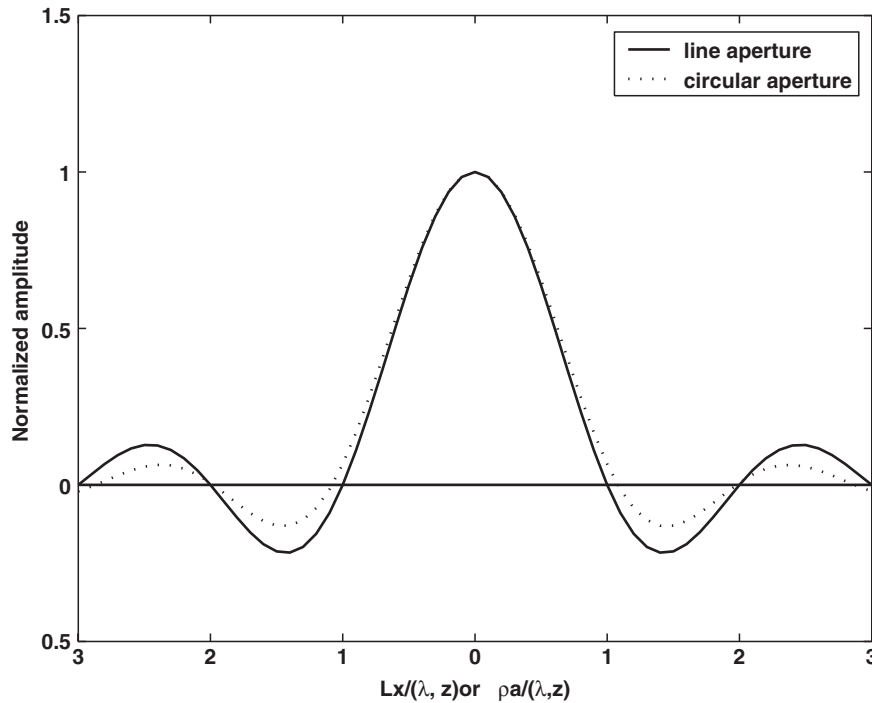


FIGURE 16.22 (a) Far-field jinc beam shape from a circular aperture normalized to (b) far-field sinc function from a square aperture with the same aperture area.

EXAMPLE PROBLEM 16.9

To understand the normalization in Figure 16.22, find the FWHM for a circular aperture having the same area as a square aperture and compare it to the FWHM of the square aperture.

Solution

Set $\pi a^2 = L^2$, or $a(m) = L(m)/\sqrt{\pi}$. Substitute in Eq. (16.45b), $\text{FWHM} = 0.7047\lambda(m)z(m) (\sqrt{\pi}/L(m)) = 1.249\lambda(m)z(m)/L(m)$. This is close to the value for the square aperture from Eq. (16.45a), $\text{FWHM} = 1.206\lambda z/L(m)$.

To narrow the beams even more and at different depths, geometric focusing is applied. Like optics, acoustic focusing can be implemented with a type of lens. Unlike optics, both concave and convex converging lenses can be made because materials exist such that their sound speeds are either greater or less than that of water (tissue). Under the principles of ray optics, the rays converge at the geometric focal point, F . From the reciprocal law of lenses, the overall total focal length is the combined effect of the natural focal length and the geometrical focal length

$$1/F_{\text{total}} = 1/F_N + 1/F \quad (16.46)$$

This relationship shows that the location of the axial peak for a focusing aperture is now moved in from the geometrical focal length. For example, if the natural focal length is 100 mm and the geometric focal length is 50 mm, the overall effective focal length is 33.3 mm. The shape of beams in the focal plane is the same as the far-field pattern of an unfocused beam; consequently, Eqs. (16.44)–(16.45) can be applied with $z = F$.

So far, solid apertures have been described. Arrays can also be considered to be spatially sampled apertures. To first order, the beams for both a solid and an adequately sampled aperture are similar. The one-dimensional array actually has two types of focusing, as shown in Figure 16.23. The azimuth or scan plane, here the x – z plane, is focused electronically, whereas the elevation or yz plane is focused by a fixed mechanical lens.

16.2.7 Ultrasound Imaging Systems

The formation of an image can be understood through the operation of an imaging system. In Section 16.2.1, an imaging system was introduced as having a transducer that could be scanned either mechanically or electronically to produce a pattern of sequential lines to form an image. With reference to Figure 16.24, the management of an array imaging system is accomplished by a computer or central processing unit (CPU). Once the scan depth and mode are selected, transmit pulses, each repeating at the time interval for a line, are sent in synchronism with a master timing clock like those in Figure 16.1. Each of these pulses initiates a set of transmit pulses from the transmit beamformer that are sent to each element, each one of which is delayed as necessary to form an electronic lens for focusing and steering the acoustic beam for the selected line direction in the azimuth plane.

Sound is scattered from tissue interfaces and inhomogeneities and is picked up as a series of pulse echoes by the array acting as a receiver. Depth-dependent time gain compensation (TGC) amplifiers can be controlled by the user to improve the image uniformity at different depths. The receive beamformer applies electronic dynamic focusing (nearly

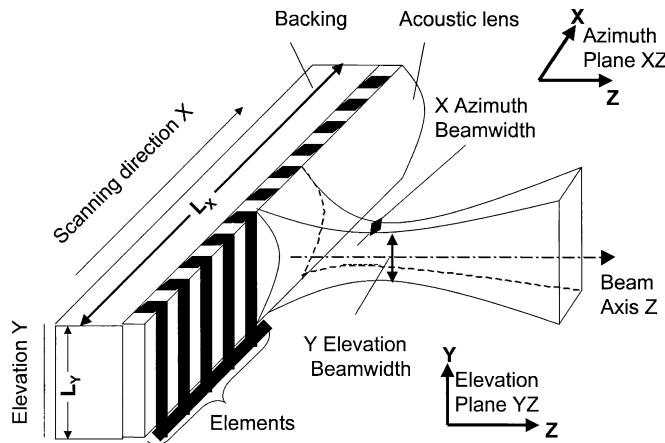


FIGURE 16.23 Focusing of a one-dimensional phased array in both the azimuth and elevation planes. Adapted from [6].

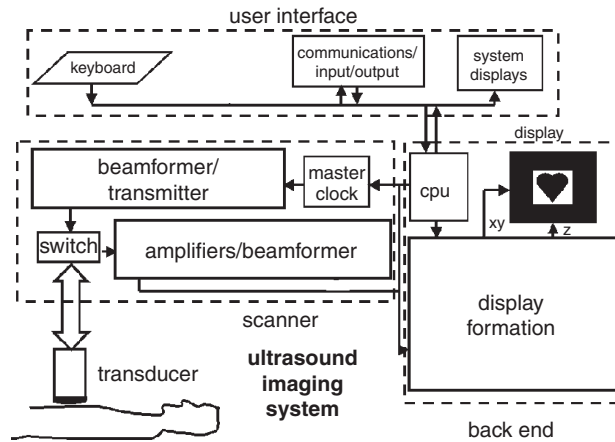


FIGURE 16.24 Block diagram of a digital ultrasound imaging system.

perfect focusing at each depth point), and signal processing (often in terms of filtering) provides the signals needed for the particular selected mode. For ordinary B-mode imaging, the envelopes of the pulse echoes are extracted, and lines containing the echoes are scan converted, the process of interpolating the lines containing pulse-echo envelopes into a filled-out, grayscale image that can be displayed on conventional PC or TV screens such as the images in [Figures 16.15 through 16.17](#). Additional steps such as log compression are used to improve the range of pulse-echo amplitudes visible on the screen. The images in [Figures 16.15](#) and [16.16](#) are of the most common type: B-mode or brightness mode.

16.2.8 Imaging and Other Modes

Other modes can supply additional information, especially about blood flow. The Doppler effect takes advantage of the apparent change in the ultrasound frequency caused by the velocity v of the blood and the angle θ the transducer makes with the vessel, as seen in [Figure 16.25](#).

The shift in frequency from the transmitted one, f_0 , or the classic Doppler shift frequency, f_D , can be expressed as

$$f_D = [2(v/c_0) \cos \theta] f_0 \quad (16.47)$$

where c_0 is the sound speed of the intervening medium. Scattering from blood is mainly from groups of red blood cells. In a vessel there is a distribution of velocities, so what is displayed is a Doppler spectrum containing frequencies corresponding to the range of sound speedsinsonified. This scattering is usually not visible by ordinary B-mode imaging but is detectable by sensitive ultrasound Doppler instrumentation. Doppler shifts are either detected along the length of an acoustic line selected to intersect a vessel of interest as continuous wave (CW) Doppler, or a small time interval is placed over the region of interest by pulsed wave (PW) Doppler as shown in the image of [Figure 16.17](#).

A more global view of blood flow, especially for the chambers of the heart and larger blood vessels, can be obtained by color flow imaging (CFI) mode. While lacking the

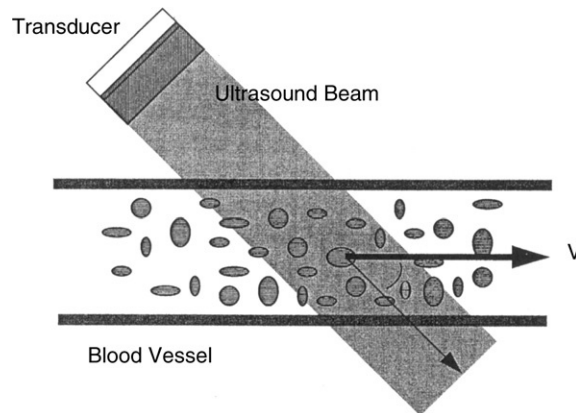


FIGURE 16.25 Sound beam intersecting blood moving at velocity v in a vessel tilted at angle θ .

precision of the Doppler modes, color flow imaging provides a real-time view of the approximate velocity and direction of blood flow. This information is represented by mapping of colors assigned to the velocity magnitude and direction (toward or away from the transducer). In this mode, several acoustic lines are sent in the same direction to obtain flow information over time, and then signal processing extracts the velocity information for display. A second type of Doppler image is called power Doppler, in which the amplitude of the flow is presented but not the direction, as illustrated by the top of [Figure 16.17](#).

Most ultrasound imaging is two-dimensional in that a picture is created in an imaging or scan plane. A three-dimensional (3D) image can be created by scanning a volume rather than a plane. By mechanically moving the array in a direction perpendicular to the imaging planes, pausing long enough to acquire each image plane, and interpolating between planes, it is possible to fill in the overall volume with image data. The 3D images can be viewed in selected cut planes through the volumes or through surface or volume rendering. For example, a common application is 3D imaging of the fetus through surface rendering, in which the boundary between the fetal skin and amniotic fluid is used to create a 3D opaque surface ([Figure 16.26](#)). Volume rendering allows internal details of organs to be visualized through transparent boundaries between organs and layers. Images can also be formed through other ways of creating a set of volume data by different mechanical scanning techniques or by complete electronic scanning by a stationary two-dimensional array.

16.3 MAGNETIC RESONANCE IMAGING

16.3.1 Introduction

Magnetic resonance has been applied successfully to medical imaging of the body because of its high water content. The hydrogen atoms in water (H_2O) and fat make up approximately 60 percent of the body by weight. Because there is a proton in the nucleus of each hydrogen atom, as the nucleus spins, a small magnetic field or moment is created.



FIGURE 16.26 3D ultrasound image of a surface-rendered fetal head. *Courtesy of Philips Medical Systems.*

When hydrogen is placed in a large static magnetic field, the magnetic moment of the atom spins around it like a tiny gyroscope at the Larmor frequency, which is a unique property of the material. For imaging, a radiofrequency rotating field in a plane perpendicular to the static field is needed. The frequency of this field is identical to the Larmor frequency, and once the atom is excited, the applied field is shut off and the original magnetic moment decays to equilibrium and emits a signal. This voltage signal, detected by the same coils used for the applied field, and two relaxation constants are sensed. The longitudinal magnetization constant, T_1 , is more sensitive to the thermal properties of tissue. The transversal magnetization relaxation constant, T_2 , is affected by the local field inhomogeneities. These constants are used to discriminate among different types of tissue and for image formation. T_1 weighted images are used most often.

Today, MRI finds widespread application in the detection of disease and surgical planning. MR images are highly detailed representations of internal anatomy. These may be called parameterized images because considerable skill is involved in adjusting the instrument to obtain images that emphasize different types of tissue contrast, the discrimination among different organ types and between healthy and pathological tissues. MRI is used to examine most of the body, including the brain, abdomen, heart, large vessels, breast, bones, as well as soft tissue, joints, cartilage, muscle, and the head and neck. It is used for both children and adults and for detecting cancer pathologies, tumors, and hemorrhaging.

An early precedent to MRI was nuclear magnetic resonance (NMR), first observed as a phenomenon by Felix Bloch and Edward Purcell and their coworkers. They discovered that

not only did precessing nuclei emit a radiofrequency (rf) signal, but a radiofrequency could also be used to control precession at the Larmor resonant frequency, and, once stopped, the nuclei would emit a detectable RF signal at the same frequency. They won a Nobel Prize in 1951 for their work.

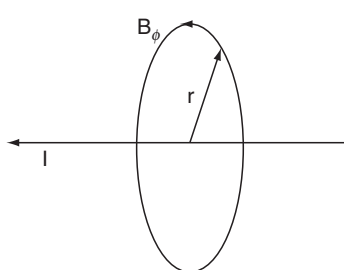
Interest shifted to determining composition of materials through unique frequency shifts associated with different chemical compounds. Eventually, biological NMR experiments were under way, and soon detailed spectral information from phosphorus, carbon, and hydrogen nuclei were obtained. Specialized magnets were designed to accommodate parts of the body for study.

Paul Lauterbur was one of the first to realize that images could be made using NMR principles. He published an image of a heterogeneous object in 1973 [4]. Using the rf signals from NMR, he was able to localize them in space by changing the magnetic field gradient. By the mid- and late 1970s, early MR images were produced of animals and the human body. At first, because the signals were so weak, these results were regarded as a laboratory curiosity. In 1971, Raymond Damadian demonstrated that the relaxation constants, T_1 and T_2 , differed for malignant tumors and normal tissue. Peter Mansfield developed a mathematical model to analyze signals from within the human body in response to a strong magnetic field, as well as a very fast imaging method. Continuous research spurred the evolution of modern MRI instruments with high signal to noise and generated a considerable knowledge base of how to apply MRI to diagnostic imaging. Lauterbur and Mansfield shared the 2003 Nobel Prize for medicine for their MRI discoveries.

16.3.2 Magnetic Fields and Charges

To understand how MRI works, several relevant characteristics of magnetic fields are reviewed here, in particular, the interactions between electrical charges and magnetic fields. Einstein pointed out that it is useful to consider electricity and electromagnetic fields as aspects of the same energy.

Four cases will be covered, each one useful for providing insights into aspects of MRI processes. In the first case, a magnetic field is generated when an alternating current travels along a wire. For an infinitely long wire, the Biot–Savart law reveals that a circular or circumferential magnetic field flux is generated by the current, as shown in Figure 16.27,

$$B_\phi = \frac{\mu_0 I}{2\pi r} \quad (16.48)$$


The diagram shows a horizontal wire with an arrow pointing to the left, labeled with the letter 'I' for current. A vertical ellipse represents a circular magnetic field loop. An arrow on the top part of the ellipse points to the left, labeled B_ϕ . A radius vector 'r' is drawn from the center of the ellipse to its upper right edge.

FIGURE 16.27 Circular magnetic field generated by an electrical current flowing down an infinitely long wire.

where the magnetic flux B is in units of Webers (1 Tesla(T) = 10^4 Webers/m²), $\mu_0 = 4\pi 10^{-7}$ Henry/m [Weber/(amp-meter)] is the permeability of free space, I is current in Amperes, and r is the radial distance from the wire in meters. The right-hand rule applies: As the fingers curl about the direction of the B field, the thumb points in the direction of the current.

EXAMPLE PROBLEM 16.10

Calculate the magnetic field in T at 5 mm from a wire carrying 20 A of current.

Solution

Using Eq. (16.48),

$$B_\phi = \frac{4\pi e - 7 \times 20}{2\pi \times 5e - 3} \text{ (Weber/m}^2\text{)} \times 1 \text{ T}/10^4 \text{ (Weber/m}^2\text{)} = 8 \times 10^{-6} \text{ T}$$

If the wire is coiled into a circular loop, a magnetic dipole with north and south poles is created. As a second case, an equivalent situation is created by a rotating charge, as shown in Figure 16.28. Current I , flowing along an increment of wire dl , in a loop is equivalent to a charge q , of mass m , orbiting at a frequency, v . The magnetic dipole moment is the product of the equivalent current and area at a large distance r ,

$$\hat{\mu} = (qvA)\hat{z} = qvpr^2 \hat{z} = \frac{1}{2}qr^2\omega\hat{z} \quad (16.49)$$

where the direction of $\hat{\mu}$ is along unit vector \hat{z} according to the right-hand rule. A vector is a quantity that has a magnitude and a direction; in this case, a unit vector has a magnitude of one and is directed along the z -axis. If the mass of the charge is m , the orbital angular momentum is

$$L = mr^2\omega \quad (16.50a)$$

The classic gyromagnetic ratio is defined as

$$\gamma_c = \frac{\mu}{L} = \frac{q}{2m} \quad (16.50b)$$

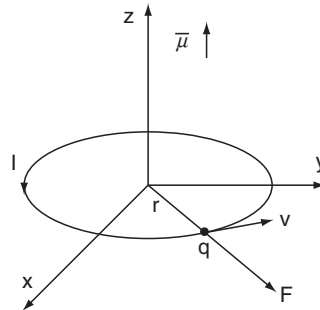


FIGURE 16.28 Magnetic dipole moment of a charge in a circular orbit.

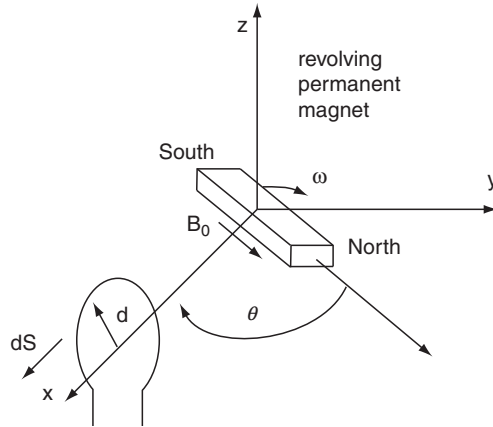


FIGURE 16.29 Voltage induced in wire loop of radius d by a revolving permanent magnet of strength B_0 .

This overall result implies that an orbiting charge can act like a small magnet with its own north and south pole.

Can a moving magnetic field create a current or voltage in a wire? For the third case, consider the arrangement in Figure 16.29, where a wire loop of radius d is perpendicular to the x -axis and where a permanent magnet of strength B_0 is whirling about the z -axis at a constant angular frequency ω . The angle between the x -axis and the magnet axis can be described as $\theta = \omega t$. Then, Faraday's law specifies that the voltage created in the loop by the spinning magnet can be written in terms of the electric field E around the loop. The area of the loop is $S = \pi d^2$, and its vector is perpendicular to the loop. If the field rotating relative to the x -axis is $B_0 \cos \omega t$ and has a direction along vector B , then according to Faraday's law,

$$V = -\frac{d}{dt}(B_0 \pi d^2 \cos \omega t) = -\omega B_0 \pi d^2 \sin \omega t \quad (16.51)$$

The voltage picked up from the rotating magnet is sinusoidal and is maximum when the axis of the magnet is perpendicular to the plane of the loop and is zero when the axis is parallel.

For the fourth case, a whirling charge is placed in a strong static magnetic field B_0 , as shown in Figure 16.30. Here, the action of the field on the charge exerts a force on the charge described by the Lorentz force equation

$$\hat{F} = q\hat{v} \times \hat{B}, \text{ or } |F| = q|v||B| \sin \theta \quad (16.52a)$$

where this vector cross-product notation means the velocity vector \hat{v} is tangential to the orbit at the position of the charge and the force is exerted outward perpendicular to both \hat{v} and the applied field direction, \hat{B}_0 and the angle between \hat{v} and \hat{B}_0 , $\theta = 90^\circ$. The magnitude of this force can be rewritten for this case as

$$|F| = q|v||B| \sin \theta = mv^2/r \quad (16.52b)$$

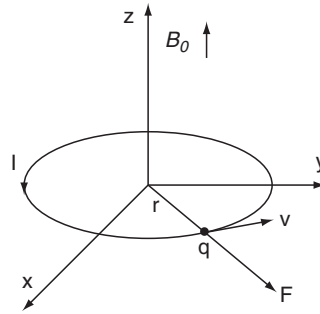


FIGURE 16.30 Lorentz force on a charge revolving about a static magnetic field. Vectors for velocity, v , force, F , and magnetic field, B_0 , are shown at the position of the charge.

The classical angular frequency of the charge can be expressed in terms of the velocity of the charge and the radius, which can be rewritten from the previous equation to give

$$\omega_c = v/r = v/(mv/qB_0) = (q/m)B_0 \quad (16.53a)$$

From the definition of the classic gyromagnetic ratio, [Eq. \(16.50\)](#), comes an important equation in MRI for the classical frequency,

$$v_c = \frac{\omega}{2\pi} = \frac{(2\gamma_c)B_0}{2\pi} = \frac{\gamma_c B_0}{\pi} \quad (16.53b)$$

which shows that the orbital frequency of the charge is proportional to the applied magnetic field. Unfortunately, this is not exactly what is needed for MRI because classical electromagnetic theory is for a charge that does not revolve on its own axis. The charge of interest in MRI is for an electron, which has its own individual spin. This situation is analogous to the revolution of the earth around the sun in combination with the revolution of the earth about its own axis. To obtain this important equation, an explanation of spin states is necessary from quantum mechanics.

16.3.3 Spin States

Based on the previous discussion, one could expect that the electron spinning on its own axis would create a miniature magnetic field; consequently, it would behave like a magnetic dipole with its own north and south poles.

Permanent bar magnets are dipoles that have a strong polarization in the form of north and south poles. If two equal permanent bar magnets are placed in the north to south setup shown in [Figure 16.31a](#), they are strongly attracted and are said to have a strong attractive force between them. If they are placed close to each other in a north–north (or a south–south) configuration as in [Figure 16.31b](#), the magnets are forced apart by a strong repulsive force. These two arrangements of magnets are two positions in which the strongest forces are stabilized in equilibrium.

If a number of the tiny magnetic dipoles are placed in a strong static magnetic field, B_0 , then they will align either with the direction of the field (parallel) or lock into a position

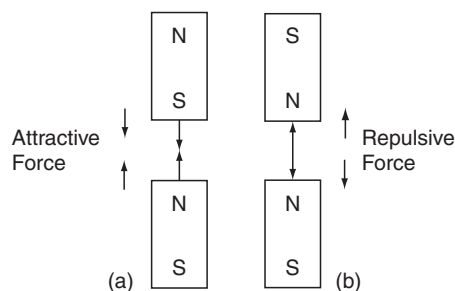


FIGURE 16.31 Attractive (a) and repulsive (b) magnetic forces for two arrangements of permanent magnets with north (N) and south (S) poles.

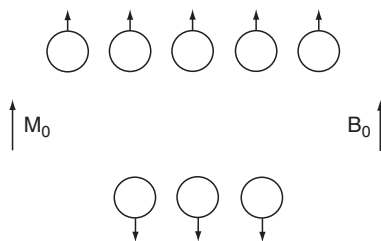


FIGURE 16.32 Alignment of magnetic dipoles in a static magnetic field B_0 and the net magnetization.

opposing the field (antiparallel), as shown in Figure 16.32. Most of them will line up along the applied field because less energy is required to maintain that orientation. The overall vector summation of the individual dipole moments results in an overall net magnetization

$$\hat{M}_0 = \sum_n \hat{u}_n \quad (16.54)$$

as shown in the figure.

The energy required for the transition from one spin state to another is governed by

$$\Delta E = \hbar v \quad (16.55)$$

in which Planck's constant is $\hbar = 6.626 \times 10^{-34} \text{ J}\cdot\text{s}$. The physical meaning of this relation is that a photon of frequency v is either absorbed to send an electron to a higher energy state or it is radiated for the electron to fall to a lower state. Eventually, excited electrons return to their original equilibrium state. Unlike x-ray imaging that emits ionizing radiation, only harmless photons are emitted during this mechanism that is used in MRI.

What is the frequency necessary for this transition? Returning to the last case of a charge revolving about the nucleus in a static magnetic field, the spin gyromagnetic ratio, γ , from quantum mechanics for a spinning electron is q/m . The orientation of the spin results in a left-hand rule (clockwise about B_0). Like Eq. (16.53b), substitution for frequency equation yields

$$v_L = \frac{\omega}{2\pi} = \frac{\gamma}{2\pi} B_0 = \gamma' B_0 \quad (16.56)$$

TABLE 16.2 Characteristics of Isotopes Relevant to MRI

Isotopes	Spin State	γ' (MHz/T)	Natural Isotopic Abundance %	Sensitivity Relative to ^1H
^1H	1/2	42.58	99.99	100
^{13}C	1/2	10.71	1.11	1.6
^{19}F	1/2	40.05	100	3.4
^{23}Na	3/2	11.26	100	9.3
^{31}P	1/2	17.24	100	6.6

which is known as the Larmor frequency that can be used to calculate the transition energy. Note that the gyromagnetic constant, γ , is associated with angular frequency, and its normalized version, γ' , with frequency. This is the important equation that connects frequency to an applied magnetic field. For the hydrogen isotope most often used in MRI, $\gamma' = 42.58 \text{ MHz/T}$. Fortunately, the values of parameters needed for MRI fall within reasonable ranges: typical frequencies are under 100 MHz and fields are 0.1 to 4 T.

The Larmor frequency is a resonance excitation frequency used for externally producing transitions in spin states. For MRI, only isotopes that have unpaired nuclear spins that are multiples of $\frac{1}{2}$ are of interest. For example, the spin state for ^1H aligned with the applied field is assigned the name “ $\frac{1}{2}$,” and has a dipole moment of $\mu_z = \gamma\hbar \times (+\frac{1}{2})$. The antiparallel state for hydrogen has a spin designation of “ $-\frac{1}{2}$ ” and has a moment of $\mu_z = \gamma\hbar \times (-\frac{1}{2})$. In Table 16.2, values of γ' are given for different isotopes. In general, $\mu_z = \gamma\hbar m$, in which m can include any of the following values, $m = 0, \dots, \pm(I - 1)$, I , where I is the spin-state number in Table 16.2.

How many of these spin states are there? If the number of spins in the low-energy state is n_- and the number of those in the higher state is n_+ , then Boltzmann statistics predict the ratio of spins in either of these two states at any given time

$$n_-/n_+ = \exp(-\Delta E/\underline{K}T) \quad (16.57)$$

where the Boltzmann constant is $\underline{K} = 1.3805 \times 10^{-23} \text{ J/K}$, ΔE is from Eq. (16.55), and T is temperature in $^\circ\text{Kelvin}$ (K).

EXAMPLE PROBLEM 16.11

Find the fraction of excess population in the spin-up (n_+) state for a frequency of 20 MHz and a temperature of 300 K.

Solution

Calculate the change in energy for a given frequency of 20 MHz from Eq. (16.55):

$$\Delta E = \hbar v = 6.626 \times 10^{-34} \text{ J} \cdot \text{s} \times 20 \times 10^6 / \text{s} = 1.325 \times 10^{-26} \text{ J}$$

From Eq. (16.57), the excess population can be written as

$$(n_+ - n_-)/n_+ = 1 - n_-/n_+ = 1 - \exp(-\Delta E/\underline{K}T) \quad (16.58)$$

Substituting the necessary values,

$$\begin{aligned} (n_+ - n_-)/n_+ &= 1 - \exp[-1.325 \times 10^{-26} \text{ J} / (1.3805 \times 10^{-23} \text{ J/K}) 300 \text{ K}] \\ &= 3.2 \times 10^{-6} \end{aligned}$$

This is a small number based on the material under examination being entirely of one type. In reality, certain types of isotopes occur more commonly than others. The ratio of one type of isotope to the total number available in percent is called the natural isotropic abundance and is listed in Table 16.2. A third relevant question is how many of these isotopes occur in the human body? The third factor is sensitivity relative to the hydrogen isotope or the equivalent number of nuclei in a field, also listed in Table 16.2. Fortunately, hydrogen is plentiful in the body, especially in fat and water.

EXAMPLE PROBLEM 16.12

Compare the isotopes ^1H , ^{13}C , and ^{31}P for imaging. Use Table 16.2.

Solution

Note that ^1H is 99.98 percent naturally abundant. ^{13}C is not, and occurs at only 1.11 percent, so this isotope is not suitable. On the other hand, ^{31}P is abundant but is difficult to detect due to its low sensitivity. Because the body is 60 percent water by weight, it is not surprising that ^1H , with its high sensitivity and abundance, is usually used for MR imaging.

16.3.4 Precession

To excite hydrogen dipoles into a number of spin states for imaging, an external magnetic field can be applied. The natural inclination for the spin magnetic dipoles to align along the z -axis makes detection by a coil difficult if the coil is placed perpendicular to the x -axis as in the fourth case from Section 16.3.2. It is necessary to find a means to bring the dipoles down into the x - y plane so they can be detected by a coil in a manner analogous to case 4. A force is required to push the dipoles into a precession, a downward spiraling orbit. This mechanism is similar to the action of gravity on a spinning top, which is initially vertical and eventually is tilted by the force of gravity into a precessing orbit and finally into a final horizontal position (Figure 16.33).

At first, the net magnetization vector, \hat{M}_0 , is aligned with the static magnetic field along the z -axis as shown in Figure 16.33a. The application of a time-varying magnetic field, B_1 , along the x -axis at the Larmor frequency causes the magnetization to precess at an angle ϕ about the z -axis at this frequency, as shown in Figure 16.33b.

To clarify what happens to \hat{M}_0 , next, it is worth introducing a reference frame notation to simplify the description. This frame will have coordinates described by a prime notation,

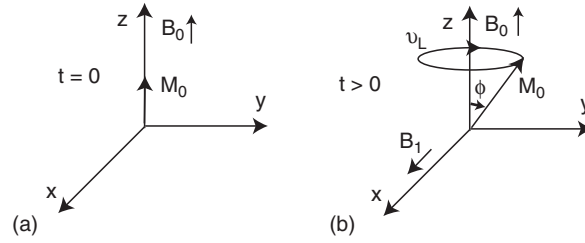


FIGURE 16.33 (a) Initial alignment of magnetization with the static magnetic field B_0 . (b) Tipping of the net magnetization from the z-axis through an angle ϕ by the application of the rf B_1 field aligned along the x-axis causes M_0 to spin about the z-axis at the Larmor frequency.

such as \hat{x}' . One reason for using this frame is that the trajectories of these spinning, precessing magnetic vectors are complicated, and simplified methods are helpful in visualizing them. Another reason is that a bundle of frequencies is usually involved in these measurements, and it is easier to track their movements relative to the reference frequency ν_L .

Rotating Frame

The approach is called a rotating frame, a coordinate frame of reference that rotates with the magnetization vector whirling at a Larmor frequency, ν_L , in contrast to a reference point in a fixed Cartesian coordinate system. This methodology is similar to a stroboscopic view-point: To make a rotating object appear still, a stroboscopic light flashes in synchronism with each revolution of the object. This light frequency serves as a reference so if the revolving object rotates faster or slower, its deviation from this reference frequency is easily seen. Similarly, a frequency rotating clockwise relative to ν_L in a rotating frame is called a positive frequency, and a frequency rotating counterclockwise is called a negative frequency.

Recall case 3 from [Section 16.3.2](#), a description of a configuration where a signal was detected from a permanent magnet spinning around the z-axis. The resulting detected signal was a sinusoidal signal with a frequency ω . Instead of a permanent magnet, consider a time-varying magnetization vector spinning at a Larmor frequency about the z-axis in the x-y plane at a position initially aligned with the x-axis at time t :

$$\hat{B}_x(t) = \hat{x}B_1 \cos \omega t \quad (16.59)$$

To find out what this magnetic field vector would look like in a rotating frame, a coordinate transformation is applied to obtain the rotated components of the field in the new frame, which are part of a new vector B'_1 with components

$$B_{x'} = \cos(\omega t)B_x - \sin(\omega t)B_y \quad (16.60a)$$

$$B_{y'} = \sin(\omega t)B_x + \cos(\omega t)B_y \quad (16.60b)$$

which with the substitution of [Eq. \(16.58\)](#) becomes

$$B_{x'} = B_1 \cos^2 \omega t \quad (16.60c)$$

$$B_{y'} = B_1 \cos \omega t \sin \omega t \quad (16.60d)$$

From trigonometric identities for half-angles, the preceding result simplifies to

$$\hat{B}'_1(t) = \hat{x}'B_{x'} + \hat{y}'B_{y'} = \hat{x}'\left(\frac{B_1}{2} - \frac{B_1}{2}\cos 2\omega t\right) + \hat{y}'\frac{B_1}{2}\sin 2\omega t \quad (16.60e)$$

which, with low-pass filtering to eliminate the components at twice the Larmor frequency, leaves

$$\hat{B}'_1(t) = \hat{x}'\frac{B_1}{2} \quad (16.60f)$$

a component of B_1 that appears to be stationary (not time varying) in the rotating frame, as expected.

Flip Angles and Decay

In MRI, the ability to control the position of the magnetization vector is important. A practical configuration to accomplish this magnetic precession is shown in [Figure 16.34](#) for rotated coordinates. First, the magnetization vector is shown aligned with the static field in [Figure 16.34a](#). Second, a radio frequency (rf) magnetic field B_1 along the x' -axis at the Larmor frequency, ν_L , is applied as a tone burst (a gated sinusoid) of pulse time duration, t_p . The application of this pulse creates a force to pull the magnetization \hat{M}_0 (usually initially aligned in an equilibrium position along the z -axis) down into a precession angle φ from the z -axis, called the flip or tip angle,

$$\varphi = \gamma\left(\frac{B_1}{2}\right)t_p = \gamma B'_1 t_p \quad (16.61)$$

The precessing magnetization vector can also be broken down into its Cartesian components in the rotated frame, as shown in [Figure 16.34b](#). In addition to the component along the z' -axis, $M_{z'}^0$, there are two components in the x' - y' plane with a radial magnitude, $M_{x'y'}^0$. It is convenient to look at the complicated resulting changes in time separately along the two components, $M_{z'}^0$ and $M_{x'y'}^0$, even though they occur simultaneously.

EXAMPLE PROBLEM 16.13

Find the pulse length necessary to achieve a phase rotation of π for the field calculated in Example Problem 16.10. Repeat for a coil that generates a field 100 times greater.

Solution

From [Eq. \(16.60\)](#), solve for t_p using [Eq. \(16.56\)](#), $\gamma = 2\pi\gamma'$, and [Table 16.2](#).

$B_1 = B_\phi = 8 \times 10^{-6}$ T from Example Problem 16.10, and $\gamma = 42.58 \times 10^6$ MHz/T. Solve for t_p in [Eq. \(16.61\)](#):

$$t_p = \frac{\varphi}{2\pi\gamma'(B_1/2)} = \frac{\pi}{2\pi \times 42.58 \times 10^6 (/s - T)(4 \times 10^{-6}T)} = 2.936 \text{ msec}$$

For the second case, the pulse is smaller by a factor of 100, or 29.36 microseconds.

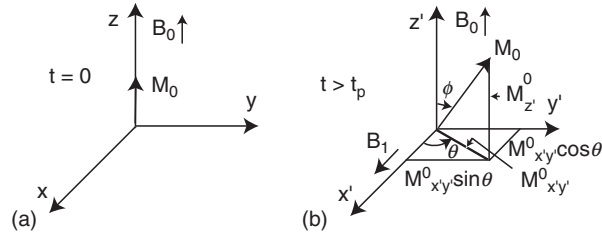


FIGURE 16.34 (a) Initial alignment of magnetization at $t = 0$. (b) Tipping of the net magnetization from the z -axis through an angle ϕ by the application of rf B_1 field at the Larmor frequency aligned along x' -axis in rotated coordinates. The projections of the net magnetization onto the axes are shown.

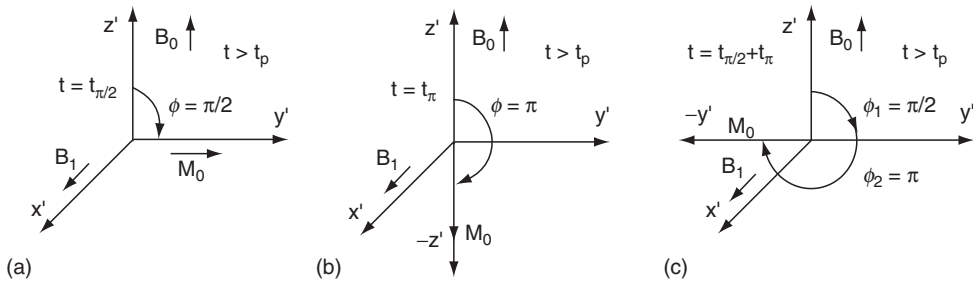


FIGURE 16.35 (a) Tipping through an angle of $\pi/2$ radians to the y' -axis. (b) Tipping through an angle of π radians to the $-z'$ -axis. (c) Tipping sequence: first tip through an angle of $\pi/2$ radians to the y' -axis and then tip through an angle of π radians to the $-y'$ -axis.

If the flip angle is chosen to be 90° or $\pi/2$ radians, the magnetization is rotated from an initial value of M_0 along the z' -axis to a position lying along the y' -axis, as shown in Figure 16.35a. The vertical component is brought a value of zero in the $x'-y'$ plane and then rebounds back to its original initial value of M_0 over a period of time. This recovery can be described by the following equation and Figure 16.36.

$$M_{z'}(\theta = \pi/2) = M_0[1 - \exp(-t/T_1)] \quad (16.62)$$

where T_1 is the spin lattice recovery time and t starts after the rf pulse. It is also called the longitudinal time constant because of its association with the vertical direction. This relaxation time is affected by temperature and the viscosity of the tissue or material (it is longer as viscosity increases).

If the flip angle is chosen to be 180° or π radians, the magnetization is rotated from an initial value of M_0 along the z' -axis to a position lying along the $-z'$ -axis. In this antiparallel orientation, the appropriate relaxation equation is

$$M_{z'}(\theta = \pi) = M_0[1 - 2\exp(-t/T_1)] \quad (16.63)$$

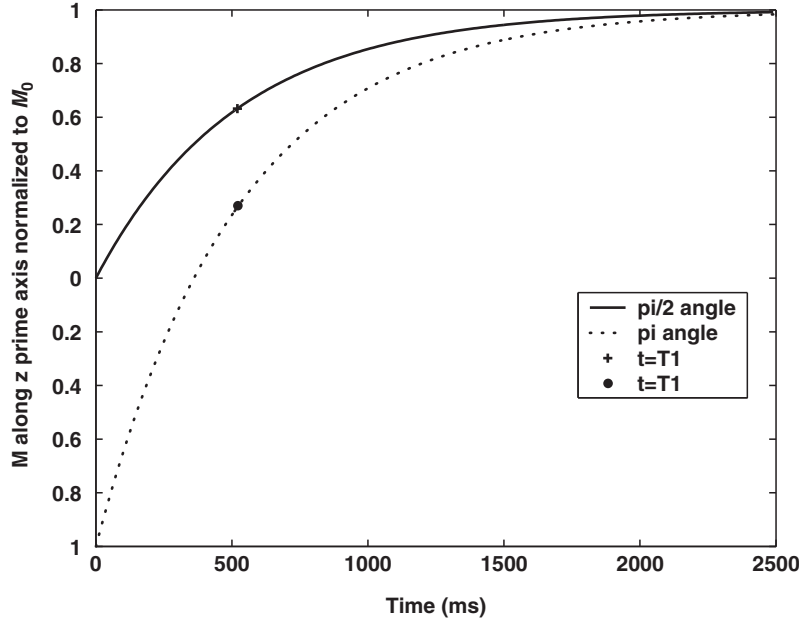


FIGURE 16.36 Plots of the recovery of a magnetization vector component along the z' -axis for a relaxation time $T_{1,s}$ versus time for a $\pi/2$ rotation, and a π rotation for gray matter of the brain.

This change is illustrated by [Figure 16.35b](#). A generalization of these equations to an arbitrary value of the z - component of magnetization following the rf pulse, M_z^0 , is

$$M_{z'}(t) = M_0 \left[1 - \left(1 - \frac{M_{z'}^0}{M_0} \right) \exp(-t/T_1) \right] \quad (16.64)$$

To determine the magnetization components in the x - y plane, refer back to the situation of the $\pi/2$ flip angle where the magnetization is rotated to the y' -axis at time $t = t_{\pi/2}$. In order for equilibrium to be restored, the initial $M_{x'y'}^0$ component at a time t beginning after the rf pulse must decay back to a zero value so the original value of the purely vertical M_0 can be recovered,

$$M_{x'y'}(\theta = \pi/2) = M_{x'y'}^0 [\exp(-t/T_2)] \quad (16.65)$$

in which T_2 is the spin-spin relaxation time as plotted in [Figure 16.37](#). Because of the motion and orientation of this component, its interaction with the material or tissue is different from that of T_1 . As [Figure 16.38](#) shows, a dephasing process occurs as vectors sweep over an increasing sector over time so the net sum of vectors gradually goes to zero.

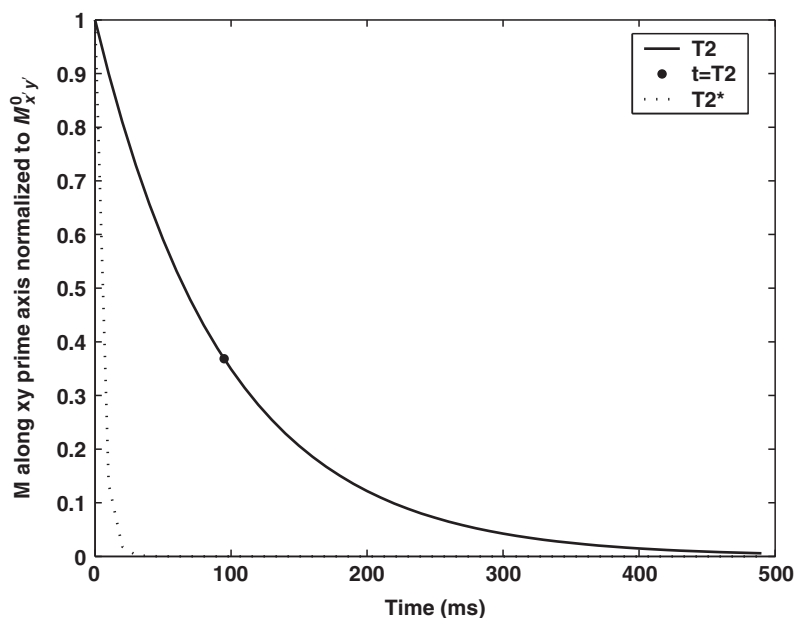


FIGURE 16.37 Plots of the magnetization vector component in the x' - y' for a decay time T_2 versus time for a $\pi/2$ rotation for gray matter and $T_2^* = 5$ ms.

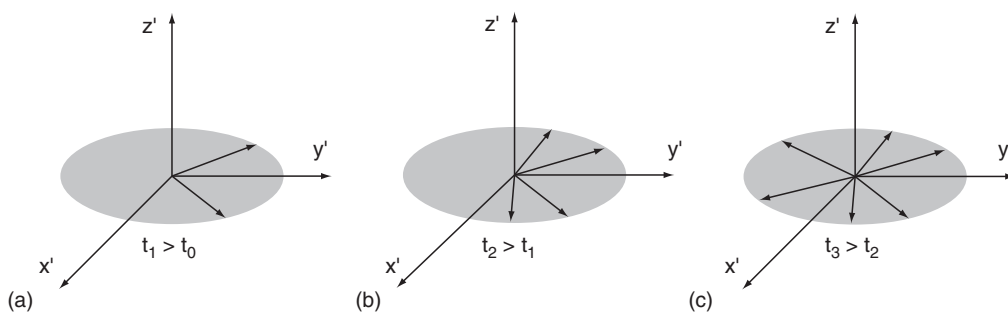


FIGURE 16.38 Time sequence of dephasing plots for spin-spin decay with time constant T_2 after $\pi/2$ rotation pulse occurring at $t = t_p$.

T_2 is sensitive to molecular interactions and inhomogeneities in the applied field B_0 . A more realistic definition of this relaxation constant includes the effects of variations ΔB_0 :

$$\frac{1}{T_2^*} = \frac{1}{T_2} + \frac{\gamma \Delta B_0}{2} \quad (16.66)$$

Through a comparison of Figures 16.36 and 16.37, it is evident that the T_2 constants are much shorter than T_1 and T_2^* is the shortest of all. Typical values for relaxation times can be found in Table 16.3.

TABLE 16.3 T_1 and T_2 Values for Common Tissue Types

Tissue	T_1 (ms)	T_2 (ms)
Cerebrospinal fluid	2,000	1,000
Fat	160	100
Gray matter	520	95
Malignant tumor	800	200
Typical edema or infarction	600	150
White matter	380	85

EXAMPLE PROBLEM 16.14

After a $\pi/2$ rotation, determine the percentage of recovery of the magnetization vertical component associated with T_1 in fat when the horizontal magnetization vector component has decayed to a $1/e$ value.

Solution

From Table 16.3, $T_2 = 100$ ms, which would be the time required for the horizontal magnetization component to decay to a value of $1/e$ value. With the value of $T_1 = 160$ ms and Eq. (16.62), the relative recovery value is

$$1 - \exp(-T_2/T_1) = 0.465$$

Detected Response Waveforms

Because sufficient background information has been given to describe the excitation and decay of a nuclear resonance, it is now possible to describe the kinds of signals detected. A setup like that of Figure 16.33a is used with a detection loop in a plane perpendicular to the x -axis. A $\pi/2$ rf excitation pulse for tipping the field 90° consists of a tone burst t_p long at the Larmor frequency according to Eq. (16.61). Since the duration of the pulse is much longer than any of the recovery and decay time constants, a sinusoidal excitation in an exponential form will be used to simplify analysis. The resulting transverse magnetization vector in the x - y plane is

$$\hat{M}_{xy}(t) = M_{xy}^0 e^{-|t|/T_2} e^{j\omega t} (\hat{x} + \hat{y}) \quad t < t_p \quad (16.67)$$

The effect of this excitation is to cause a resonance and a change in the spin states of hydrogen electrons. Faraday's law can be applied to the detection of the overall net magnetization response from Section 16.3.2, case 3. The area S of a loop of diameter d can be rewritten in terms of magnetization M and an equivalent current I :

$$S = \frac{M}{I} \quad (16.68)$$

If the direction of the area is taken to be the x' -axis and the corresponding component of M is used in Faraday's law, Eq. (16.51), for the cubic volume, V_{voxel} , of an image voxel

$$v(t) = -V_{\text{voxel}} \frac{\partial}{\partial t} \left[B'_1(t) \times \frac{M_{xy}}{I} \right] \quad (16.69a)$$

$$v(t) = -V_{\text{voxel}} \frac{\partial}{\partial t} \left[B'_1(t) \times \frac{\hat{M}_{xy}}{I} \right] = -V_{\text{voxel}} \frac{\partial}{\partial t} \left[|B'_1(t)| \left| \frac{M_{xy}}{I} \right| \sin\theta \right]$$

From Eq. (16.67) for M_{xy} and Eq. (16.60f) for $\hat{B}'_1(t)$, and since the angle between \hat{B}'_1 and \hat{M}_{xy} is $\theta = 90^\circ$, the voltage becomes

$$v(t) = \left(\frac{B_1}{2I} \right) \cdot \left(j\omega V_{\text{voxel}} M_{xy}^0 e^{-|t|/T_2} e^{j\omega t} \right) \quad (16.69b)$$

where V_{voxel} is the cubic volume of an image voxel and the second-order terms in dM/dt are dropped. This detected voltage is called the free induction decay (FID), the real part of which is shown in Figure 16.39.

The major reason the FID waveform is unsuitable for detection is that it is severely affected by variations in the magnetic field that dominate the response over the signals of the desired spin states. Also, the waveform weakens rapidly with the shorter time decay constants. As shown in Figure 16.38, spin states experience different magnetic fields because of their spatial location; therefore, the angular frequencies of their magnetization vectors vary, some moving faster than others, according to Eq. (16.56).

A clever alternative is called the spin echo method. If a certain time, $T_e/2$, elapses so that the spin vectors are severely but not totally dispersed, as shown in Figure 16.35c, a second π pulse with an amplitude twice that of the original $\pi/2$ pulse rotates the leading vectors back to the $+y$ -axis, as shown in Figure 16.40a. The individual magnetization vectors rotate in an opposite direction toward realignment. As the vectors draw into coherent phase, the detected signal increases to an alignment peak at T_e and then decays, as shown in the spin echo waveform in Figure 16.40b. The beauty of this approach is that the effects of magnetic field variations are canceled out, resulting in a truer T_2 tissue response. Following a derivation similar to that of the FID waveform, we can obtain an expression for the spin echo:

$$v(t) = j(B_1/2I)\omega V_{\text{voxel}} M_{xy}^0 e^{-|t|/T_2} e^{j\omega t} \quad (16.70)$$

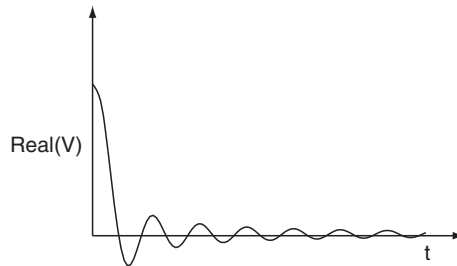


FIGURE 16.39 Free induction decay waveform versus time. This waveform starts at $t = 0$.

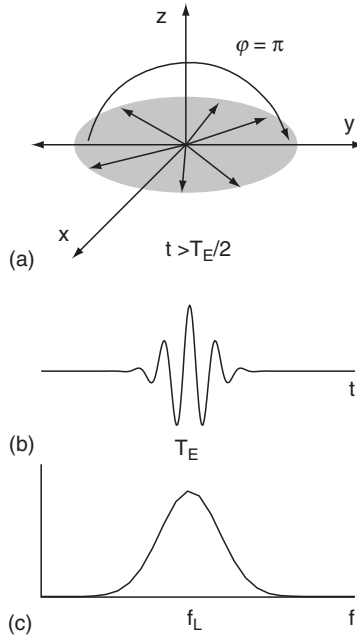


FIGURE 16.40 (a) A π pulse rotation causes a reversal in the rotation direction of the magnetization vectors so they move toward realignment: (b) spin echo waveform versus time, and (c) spin echo spectral magnitude versus frequency.

To find the spectrum of the spin echo, we use the following transform pair

$$\Im[\exp(-|t|)] = \frac{2}{1 + (2\pi f)^2} \quad (16.71a)$$

along with the transform pair for the exponential (note in Eq. (16.70), $\omega = \omega_L = 2\pi f_L$, a constant, the electrical frequency corresponding to the physical Larmor frequency),

$$\Im(e^{j\omega_L t}) = \delta(f - f_L) \quad (16.71b)$$

and the scaling theorem, Eq. (16.4a), to obtain the echo spectrum of Eq. (16.70)

$$V(f) = \Im\left(\frac{jB_1 M_{xy}^0 \omega_L V_{\text{oxel}} e^{-|t|/T_2} e^{j\omega_L t}}{2I}\right) = \frac{jB_1 M_{xy}^0 \omega_L V_{\text{oxel}} T_2}{2I} \left\{ \frac{1}{1 + [2\pi T_2(f - f_L)]^2} \right\} \quad (16.71c)$$

and the magnitude of which is shown in Figure 16.39c. If a function $S(f)$ is defined as

$$S(f) = \frac{jB_1 M_{xy}^0 \omega_L V_{\text{oxel}} T_2}{2I} \left\{ \frac{1}{1 + [2\pi T_2 f]^2} \right\} \quad (16.71d)$$

then the right-hand side of Eq. (16.71c) becomes

$$V(f) = S(f - f_n) \quad (16.71e)$$

in which $f_n = f_L$ for this case. In general, the index n can be associated with the excitation Larmor frequency at a location x_n . How this mapping is carried out is the subject of the next section.

16.3.5 Setup for Imaging

To create images from detected signals, a means of spatially localizing the detected waveforms must be used. Three methods are used to encode the waveform data and position, one for each Cartesian coordinate. The three-dimensional image is discretized into tiny cubes called voxels, each with a volume $V_{\text{oxel}} = \Delta x \Delta y \Delta z$.

The first step in setting up the image is to fix the desired location of the slice plane, one voxel thick, along the z -axis, as shown in Figure 16.41. The person to be imaged is slid into a large superconducting magnet that creates a strong static field, B_0 . Recall from cases 1 and 2 from Section 16.3.2 that a current in a wire or loop can generate a magnetic field. Electrical coils are arranged within the magnet to create an electrically controlled linear magnetic field gradient along the z -axis

$$\vec{B}_z = \hat{z}(B_0 + G_z z) \quad (16.72a)$$

where G_z is a gradient constant in T/m . From Eq. (16.56), a unique Larmor frequency is associated with each spatial location z ,

$$\omega = \gamma B_z = \gamma B_0 + \gamma G_z z \quad (16.72b)$$

The relative position $z = 0$ is called the isocenter. The reference frequency associated with this center is $\omega_0 = \gamma B_0$, which can be subtracted from ω by electronic mixing.

By applying a time excitation pulse with an appropriate center frequency as shown in Figure 16.41, a specific location is selected. The envelope of the sinusoid used for time

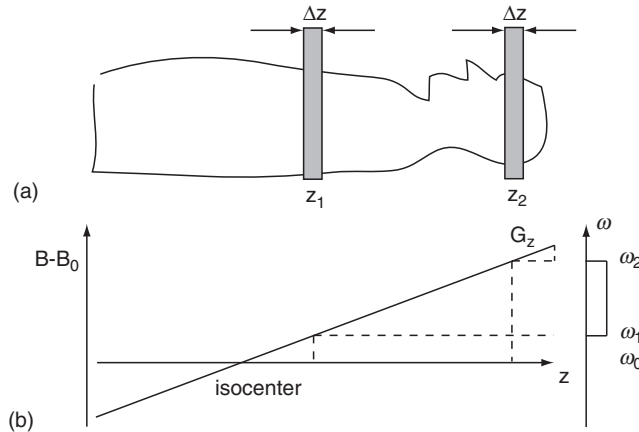


FIGURE 16.41 (a) Side view of selected axial image plane locations. (b) Two regions corresponding to selected locations on the z -axis magnetic field gradient. On the right vertical axis are regional gradient spectra from rf excitation pulses whose Larmor center frequencies are selected for z -axis positions. Scale is exaggerated for clarity.

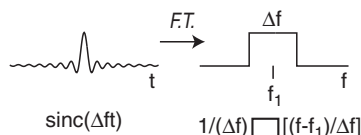


FIGURE 16.42 Sinc modulated excitation pulse with a selected Larmor center frequency and its Fourier transform representing its spectrum or the shape of the applied field.

domain rf pulse excitation is shaped to obtain a flatter field. A sinc-shaped pulse would have a flat rectangular spectral shape, a consequence of its Fourier transform relation, but, ideally, it would have to be infinitely long. This pulse and the corresponding field-spectral shape are shown in Figure 16.42. A sinc-time pulse has a Fourier transform, \mathfrak{F} , that can be expressed as a rect function of width Δf :

$$\mathfrak{F}[\sin c(\Delta ft) \exp(j2\pi f_1 t)] = (1/\Delta f) \Pi[(f - f_1)/\Delta f] \quad (16.73)$$

As a compromise, a truncated or tapered or modified sinc pulse of finite length is applied instead, such as the tapered shape shown in Figures 16.40b and 16.40c.

EXAMPLE PROBLEM 16.15

Find the bandwidth needed to achieve a z-slice thickness of 10 mm. Assume $G_z = 0.352 \text{ T/m}$. For $B_0 = 1\text{T}$, determine the frequencies needed to move 10 cm and 20 cm from the isocenter.

Solution

From a version of Eq. (16.72b) with γ' , the difference in frequency is proportional to thickness, or

$$\Delta f = 42.58(\text{MHz/T}) \times 0.352(\text{T/m}) \times .010 \text{ m} = 0.15 \text{ MHz}$$

The same equation can be used with a value of the offset from the isocenter, $f_1 = 42.58 \text{ (MHz)} [1\text{T} + 0.352 (\text{T/m}) \times 0.1 \text{ m}] = 44.08 \text{ MHz}$. Similarly, $f_2 = 45.58 \text{ MHz}$ corresponds to the frequency needed to move 20 cm from the isocenter.

In order to scan the x - y slice plane located by the z -axis gradient control, as seen in Figure 16.43, the second step is to locate data points along the axis. A gradient is also applied along the x -axis for spatial localization,

$$\omega = \gamma B_x - \gamma B_0 = \gamma G_x x \quad (16.74a)$$

Again, with mixing, $\omega_{\text{mix}} = \omega_0$ for $B = B_0$, the difference frequency is proportional to the position x ,

$$\omega_\Delta = \omega - \omega_{\text{mix}} = \gamma G_x x \quad (16.74b)$$

For z slice selection, a specific frequency is applied that corresponds to a particular desired location, according to Eq. (16.72b). Although a similar principle is used for the locations along x , the implementation is somewhat different. Here, the detected signal

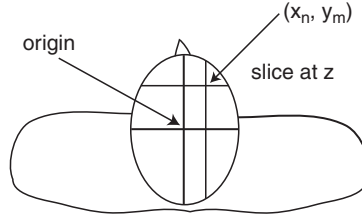


FIGURE 16.43 Depiction of an x - y slice plane of thickness Δz at a distance z , like the positions shown in Figure 16.41.

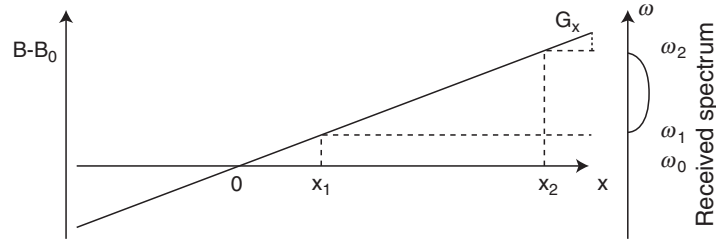


FIGURE 16.44 Frequency encoding method for x -axis with two locations, x_1 and x_2 , shown.

frequency varies with distance x , a consequence of the linear magnetic field gradient, as shown in Figure 16.44. A number of excited resonances positioned along the scan line x can contribute to the overall detected signal and are encoded in the received signal as different frequencies.

Unlike diagnostic ultrasound imaging in which specific echo delays in time are associated with reflectors at different round-trip distances, MRI signals for different spatial locations are frequency encoded and added together in the same time signal position. In this case,

$$V(f) = \sum_n S(f - f_n) \quad (16.75)$$

The means of decoding these positions will be explained in a later section. Although MRI systems have employed yet another linear magnetic gradient along the y -axis to provide localization for this coordinate, a different phase-encoding scheme is now more common. The mechanism employed is that of the flip angle, Eq. (16.61), with a different twist

$$\phi(y) = \omega t = -(\gamma B_0 t + \gamma G_y t_p y) \quad (16.76)$$

in which $y = y' + y_0$, where y_0 is the value at the center. In the previous discussion of the flip angle, an rf magnetic field with an appropriate pulse width, t_p , was applied to the spins to rotate a magnetization vector through a desired angle. In this context, Eq. (16.76) shows that either the pulse length, t_p , or the pulse gradient slope, G_y , can be used to change the phase.

The preferred method, as shown in Figure 16.45, is not to change pulse widths but rather to alter amplitudes and signs of the gradient slope, which can be changed by voltage amplitudes applied to the y -axis gradient coil. In order to fill out the x - y plane, a means of

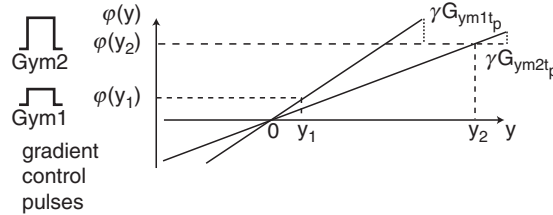


FIGURE 16.45 Phase encoding method for the relative y -axis for two locations, y_1 and y_2 .

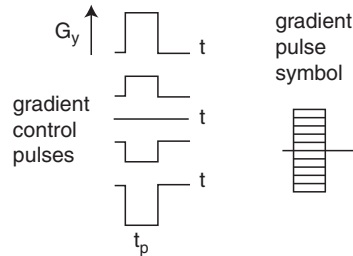


FIGURE 16.46 Pulse sequences for several consecutive lines. Note the amplitude of G_y pulses changes on sequential lines. TR is the repetition time between lines. Usually the amplitudes for G_y range from a maximum value, $G_{y\max}$, through a negative value of the same magnitude.

scanning along y is needed. Typically, 128 or 256 different excitations are utilized, and each one has to be uniquely linked with a specific y position. Pulse and excitation sequences for several consecutive lines are shown in [Figure 16.46](#).

16.3.6 The Magnetic Resonance Imaging Sequence

Almost all the necessary bits and pieces needed for the imaging process have been introduced. Now, step by step, the different controls and detection methods will be reviewed and assembled into a sequence of events for imaging. The process will be simplified slightly for clarification. [Figure 16.43](#) shows an x - y image plane that contains the isocenter, or center of magnetic field coordinate system, for a head scan. How net magnetization signals from specific locations in this plane translate into magnetic fields, detected waveforms, and ultimately into an image will be demonstrated.

Once the subject is within the MRI magnet, a series of sequence pulses are sent, as shown in [Figure 16.47](#). In the figure, two rf pulses, one a $\pi/2$ pulse and one a π pulse, force the magnetization vectors to precess into the x - y plane to set up spin echoes, as described in [Section 16.3.4](#). The G_{zz} -axis gradient pulses occur over the same intervals as the rf pulses. They turn on the gradient coils, which, in combination with the frequency selected for the rf pulses, select the z location of the x - y image plane, as detailed in [Section 16.3.5](#).

The gradient pulses for the x -axis occur during the precession phase and also over the interval during which the spin echoes are formed. The field must be on during these

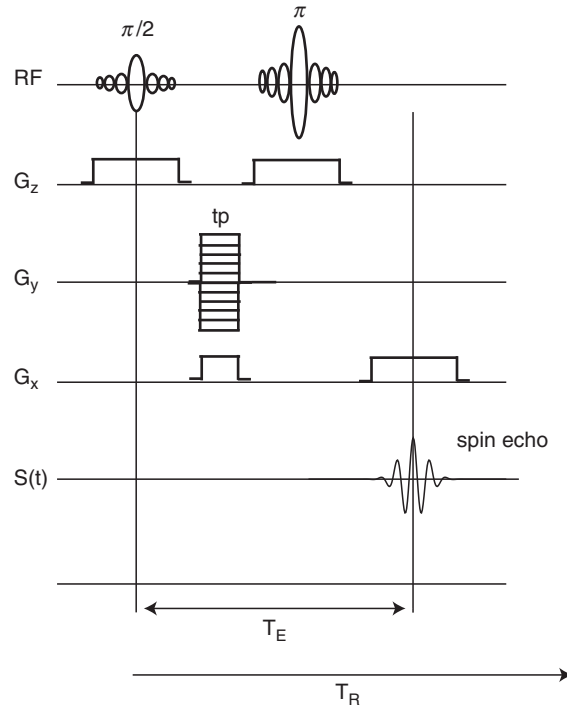


FIGURE 16.47 Essential rf excitation, and gradient pulse sequences, G_z , G_y , G_x , for spin-echo detection, $s(t)$.

intervals so the positions of the spins are translated into different frequencies that vary with position along the x -axis. Finally, a y gradient pulse excites the coils along the y -axis with an amplitude appropriate to phase encode the position y . Spin echoes are sensed at $t = T_E$. The sequence is repeated at intervals of T_R .

To form an image, the set of acquired signals and the object to be imaged (a distribution of net magnetization vectors) are assumed to be related by Fourier transforms. If a particular slice plane has been selected at z , then the object is a function of position (x, y) , which implies that a double Fourier transform (for two dimensions) is involved. It will be easier to consider each dimension separately (x or y) and then combine them into a 2D transform. Signals detected from a net magnetization distribution at a position (\underline{x}_n, y_m) will be considered.

Before starting with the y -axis, it will be helpful to review the role of the impulse in Fourier transform theory described in [Section 16.2](#). The impulse and its transform play an essential role in the understanding of MRI. The impulse function is a generalized function that has the unusual property of sampling the integrand, as introduced in [Section 16.1.1](#):

$$\int_{-\infty}^{\infty} \delta(f - f_0) R(f) df = R(f_0) \quad (16.77a)$$

When the inverse Fourier transform of the impulse function is taken, the result is an exponential

$$g(t) = \int_{-\infty}^{\infty} \delta(f - f_0) e^{i2\pi f t} df = e^{i2\pi f_0 t} \quad (16.77b)$$

which has the forward Fourier transform

$$G(f) = \int_{-\infty}^{\infty} (e^{i2\pi f t_0}) e^{-i2\pi f t} dt = \int_{-\infty}^{\infty} e^{i2\pi t(f - f_0)} dt = \delta(f - f_0) \quad (16.77c)$$

If $w(t)$ has the Fourier transform $W(f)$, then

$$\int_{-\infty}^{\infty} [w(t) e^{i2\pi f t_0}] e^{-i2\pi f t} dt = \int_{-\infty}^{\infty} w(t) e^{i2\pi t(f - f_0)} dt = W(f - f_0) \quad (16.77d)$$

The simplest place to start is the y -axis. For the y dimension, phase encoding according to Eq. (16.76) is applied and expressed with the constant phase term suppressed after mixing,

$$\varphi(y) = -\gamma G_y t_p y \quad (16.78a)$$

The phase associated with a particular location is

$$\Phi_m(y_m) = -(\gamma G_{y,m} t_p y_m) \quad (16.78b)$$

where the phase is indexed to a position y_m as well as a specific gradient slope coefficient, $G_{y,m}$. The encoded time signal can be described by

$$s_m(0, G_y) = e^{-i\gamma t_p y_m G_y} \quad (16.78c)$$

The Fourier transform pair of variables for the y dimension will be the varying amplitude slope, G_y , as indicated in Figure 16.45 and a new variable called u . Analogous to the paired variables t and f , which have reciprocal units, u will have the upside-down or inverse units of m/T . These variables, G_y and u , can be used to construct a specific phase term that later will be associated with y_m in a Fourier transform format:

$$S_m(0, u) = \int_{-\infty}^{\infty} (e^{i2\pi u y_m G_y}) e^{-i2\pi u G_y} dG_y = \int_{-\infty}^{\infty} e^{-i2\pi(u - u_m) G_y} dG_y = \delta(u - u_m) \quad (16.79)$$

Here, u appears in the argument of the second exponent in the integrand. The overall argument is recognized as a phase according to Eqs. (16.77c) and (16.78a) so an explicit expression for u can be obtained by equating phases:

$$2\pi u G_y = -\gamma t_p y G_y \quad (16.80a)$$

$$u = -\gamma t_p y / (2\pi) \quad (16.80b)$$

This evaluation of the Fourier transform of phase encoding follows directly from the discussion of the impulse function. As a consequence of this change in variables, the spectrum S_m in Eq. (16.79) can be restated in terms of the scaled variable from Eq. 16.80b,

$$S_m(0, u) = \delta(u - u_m) = \delta[(-\gamma t_p / (2\pi))(y - y_m)] \quad (16.81a)$$

$$S_m(0, y) = [2\pi / \gamma t_p] \delta(y - y_m) \quad (16.81b)$$

where use has been made of the property $\delta(au) = \delta(u)/|a|$ from Section 16.2.

The derivation of this key equation reveals an important principle in magnetic resonance imaging. First, a local value of a gradient slope, G_{y_m} , encodes a position, y_m , into a phase according to Eq. (16.78b). Second, this phase, in terms of Fourier transforms, ensures that the signal function has a spectrum centered on the value of u associated with the location of the corresponding net magnetization. Through simple scaling, the scaled spectra are translated into spatial locations along the y -axis (Figure 16.48a). This process maps a scaled spectral magnitude into its locations along the y -axis.

To formulate the Fourier transform relation for the x -axis, a single spin echo waveform is generated, for example, at the position $y = 0$ in Figure 16.40b, so that $G_y = 0$. From Eq. (16.70), the signal waveform, delayed by time T_E and decaying with a unique time constant T_{2n} associated with location x_n can be expressed as

$$s_n(t, 0) = 2S_0 e^{-|(t-T_E)/T_{2n}|} e^{j\omega_n(t-T_E)} \quad (16.82)$$

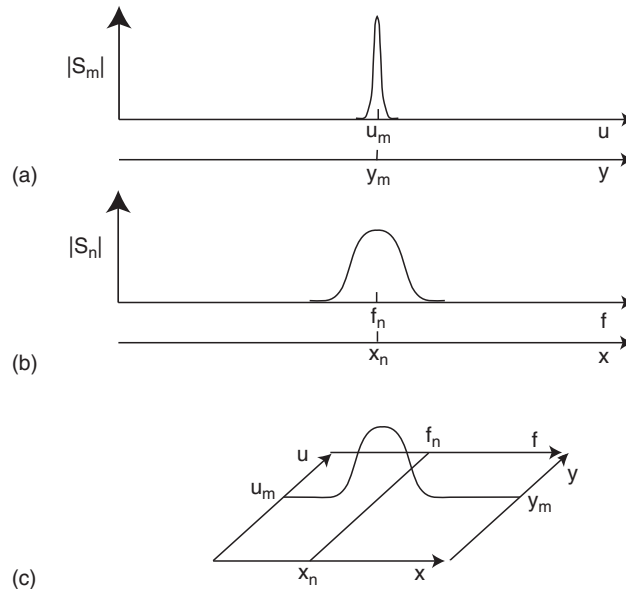


FIGURE 16.48 (a) Spectrally phase-encoded magnitudes plotted versus multiple scaled y - and u -axes. (b) Spectral frequency-encoded magnitudes plotted versus multiple scaled x - and f -axes. (c) Resulting pattern in xy or uf plane. Scale exaggerated for clarity.

in which the s is a function of t and $G_y = 0$, S_0 is a constant, and the Larmor frequency associated with location x_n is

$$\omega_n = \gamma G_x x_n \quad (16.83)$$

after mixing removes ω_0 at the isocenter.

The one-dimensional Fourier transform of Eq. (16.82) is

$$S_n(f, 0) = \int_{-\infty}^{\infty} s(t, 0) e^{-i2\pi f t} dt = \int_{-\infty}^{\infty} \left[S_0 e^{-|t-T_E|/T_{2n}} \right] \left[e^{-i2\pi f_n T_E} e^{-2\pi(f-f_n)t} \right] dt \quad (16.84a)$$

The form of the complex exponents is recognizable from Eq. (16.77d) as the transform of an impulse function centered on f_n . This relation implies that the Fourier transform of the function in the left brackets is centered on f_n . To show this result, it is necessary to determine if the Fourier transform of the first term in brackets is of the form of Eqs. (16.71a) and (16.71d) with S_0 as the constant,

$$W_n(f, 0) = \int_{-\infty}^{\infty} w_n(t, 0) e^{-i2\pi f t} dt = \int_{-\infty}^{\infty} \left[S_0 e^{-|t-T_E|/T_{2n}} \right] e^{-i2\pi f t} dt = \frac{S_0}{1 + (2\pi f T_{2n})^2} \quad (16.84b)$$

then $S_n(f, 0)$ can be expressed as

$$S_n(f, 0) = e^{-i2\pi f_n T_E} W_n(f - f_n) \quad (16.84c)$$

From the relation for the Larmor frequency, this equation can be rewritten in terms of a scaled variable for frequency from Eq. (16.83) as

$$S_n(x, 0) = e^{-i\gamma G_x x_n T_E} W_n \left[\frac{\gamma G_x}{2\pi} (x - x_n) \right] \quad (16.84d)$$

The derivation of this key equation reveals a second important principle in magnetic resonance imaging. First, a locally excited resonance encodes a position into a frequency f_n as part of the phase of a time waveform. Second, this phase, in terms of Fourier transforms, ensures that the signal function has a spectrum centered on the frequency associated with the location of the net magnetization density. Third, through simple scaling, the scaled spectra are translated into spatial locations along the x -axis (Figure 16.48b). This process maps scaled spectral magnitudes into their spatial locations along the x -axis.

To advance to two dimensions, the one-dimensional inverse Fourier transforms are combined in a two-dimensional relation:

$$s(t, G_y) = \mathfrak{F}^{-1}[I(f, u)] = \iint I(f, u) e^{i2\pi f t} e^{i2\pi u G_y} df du \quad (16.85)$$

To find the object distribution, I , from the measured set of signals from a location (x_n, y_m) , a forward 2D Fourier transform is

$$I(f, u) = S_{mn}(f, u) = \mathfrak{F}[s_{mn}(t, G_y)] = \iint s_{mn}(t, G_y) e^{-i2\pi f t} e^{-i2\pi u G_y} dt dG_y \quad (16.86)$$

If the set of signals is taken to be simply the product of the one-dimensional signals for this simplified example

$$s_{mn}(t, G_y) = \left[S_0 e^{-|(t-T_E)/T_{2mn}|} e^{j\omega_n(t-T_E)} \right] e^{i2\pi y_m G_y} \quad (16.87)$$

then inserting this set into the 2D transform of Eq. (16.86) yields

$$S_{mn}(x, y) = \left\{ e^{-i\gamma G_x x_n T_E} W_{mn} \left[\frac{\gamma G_x}{2\pi} (x - x_n) \right] \right\} [2\pi/(\gamma t_p)] \delta(y - y_m) \quad (16.88)$$

In this case, as depicted in Figure 16.48c, the intersection of these one-dimensional functions places a scaled spectrum at the location (x_n, y_m) . The role of u_m is to localize the position of the spectrum along y through scaling. In an MRI image, this spectrum, S_{mn} , is displayed as amplitude mapped on a gray scale with full white as maximum amplitude in the image plane at location z . What are displayed, then, are not the detected time signals but the amplitudes of their spectra, which through encoding methods are mapped into their proper spatial locations from anatomy.

In reality, during actual measurements, what are sensed are the signals from all the active net magnetization vectors from all the locations being scanned. The detected voltage is the sum of all the signals picked up in a specific z plane

$$V(t, G_y) = \sum_{m,n} s_{m,n}(t, G_y) \quad (16.89)$$

where the signals are not the ideal forms derived in Eqs. (16.87) and (16.88) but signals reflecting the characteristics and organization of tissue structures.

A convenient way of discussing the signals in terms of Fourier transforms is to describe the acquired signals as belonging to a k -space domain and the transformed signals as being in the space (x, y) domain. As shown in the following, this perspective is simply accomplished as a change in variables in the previous transform equations. The simplest place to start is in the exponential arguments of the transform equations, Eqs. (16.83) and (16.80a), that contain the key variables. These variables are set equal to the desired new ones:

$$2\pi f_n t = k_x x_n \quad (16.90a)$$

$$2\pi u G_y = k_y y_m \quad (16.90b)$$

From previous definitions, it is straightforward to show that

$$k_x = \gamma G_x t \quad (16.91a)$$

$$k_y = -\gamma G_y t_p \quad (16.91b)$$

or

$$t = k_x / \gamma G_x \quad (16.92a)$$

$$G_y = -k_y / \gamma t_p \quad (16.92b)$$

Equations (16.92a) and (16.92b) can be substituted in Eq. (16.85) to yield

$$s(k_x / \gamma G_x, -k_y / \gamma t_p) = \iint \left\{ \left(\frac{\gamma G_x}{2\pi} \right) \left(\frac{-\gamma t_p}{2\pi} \right) I \left[\left(\frac{\gamma G_x}{2\pi} \right) x, \left(\frac{-\gamma t_p}{2\pi} \right) y \right] \right\} e^{ik_x x} e^{ik_y y} dx dy \quad (16.93)$$

or by redefining the functions in terms of the new variables, \tilde{s} and \tilde{I} ,

$$\tilde{s}(k_x, k_y) = \iint \tilde{I}(x, y) e^{ik_x x} e^{ik_y y} dx dy \quad (16.94)$$

where $\tilde{I}(x, y)$ is equal to the term in the braces outside the exponentials in Eq. (16.93) and \tilde{s} is redefined as well. Similarly, Eq. (16.86) becomes

$$\tilde{I}(x, y) = \iint (\tilde{s}(k_x, k_y) e^{-ik_x x} e^{-ik_y y} dk_x dk_y \quad (16.95)$$

Previous results have now been recast in xy -space and k -space variables.

16.3.7 Magnetic Resonance Imaging Systems

The main parts of an MRI system are shown in Figure 16.49. A large superconducting magnet provides a homogeneous static B_0 magnetic field within its interior. Typical clinical field values vary from 0.15 to 2 T, but there are systems available in the 3 to 5 T range. Inserted within the main magnet are pairs of surface coils for producing the x -, y -, and z -axis gradients. These typically produce variations of only a few percent of the value of the static field for spatially localizing the magnetic spin signals of the body. These signals are picked up by rf transmit/receiver coils that are sometimes in the form of surface coils placed close to the body. The rf signals are directed by a computer (CPU) through the rf pulse generator and sequencer and sequencer. A switch routes the received rf signals through an amplifier and into a data acquisition unit, after which they are processed and Fourier transformed to create an image. Modern systems allow the operator considerable flexibility to alter the gradients and pulse sequences to achieve different image effects and weighting. Typical image acquisition times are on the order of 50 to 100 ms, though faster acquisitions are becoming available.

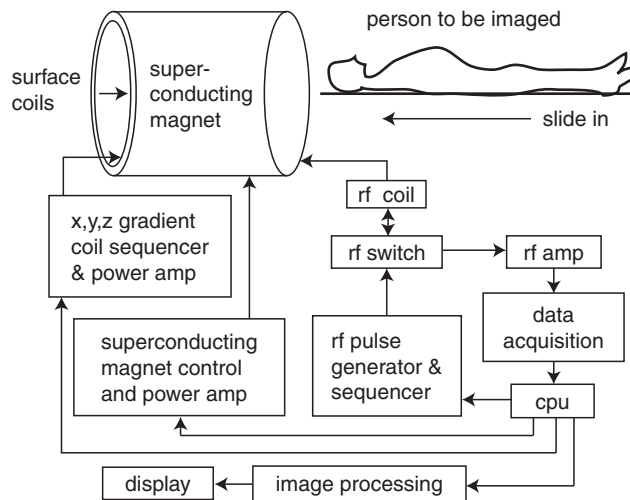


FIGURE 16.49 Block diagram of an MRI system.

Different signal characteristics can be emphasized by a manipulation of the basic pulse timing sequences (see Figure 16.47). For example, a short pulse repetition interval, TR , and a short spin echo time, TE , results in the commonly used T_1 weighting (T_1W) shown in Figure 16.50b. For example, typical values are $TE = 12$ ms and $TR = 300$ ms. Prolonging TR and the delays before and after TE produces a T_2 -weighted (T_2W) image as in Figure 16.50a. An example of this is $TE = 100$ ms and $TR = 3,000$ ms. A combination of a long TR and a short TE creates what is called a proton density weighted (PD) image, shown in Figure 16.50c. For example, typical values are $TE = 30$ ms and $TR = 3,000$ ms. Recall that T_1 is more sensitive to local thermal properties and T_2 depends more on local transverse magnetic field inhomogeneities. Many other alternative timing and pulse sequences are possible and are useful for different clinical applications.

An important aspect of imaging is contrast among different types of tissues. In Figure 16.51 longitudinal magnetization is shown for two tissues as a function of time, indicating their different T_1 rise times. Note that the contrast among the tissues varies at different times, as indicated by the vertical separation between the curves at different times. For example, compare the separations for times of 400 ms, 800 ms, and 1,600 ms. Here it can be seen that contrast can be changed by timing intervals. Another way of enhancing contrast is to inject a paramagnetic medium or contrast agent such as gadolinium.

16.3.8 Magnetic Resonance Imaging Applications

Functional MRI (fMRI) is the use of MRI to detect localized changes in brain activity, usually in the form of changes in cerebral metabolism, blood flow, volume, or oxygenation in response to task activation. These changes are interrelated and may have opposite effects. For example, an increase in blood flow increases blood oxygenation, whereas an increase in metabolism decreases it. The most common means of detection is measuring the changes in the magnetic susceptibility of hemoglobin. Oxygenated blood is dimagnetic and deoxygenated blood is paramagnetic. These differences lead to a detection method called blood oxygen level dependent contrast (BOLD). Changes in blood oxygenation can be seen as



FIGURE 16.50 MR images of sagittal brain cross sections using three types of weighting planes: (a) T_2 , (b) T_1 , and (c) proton density. Courtesy of Philips Medical Systems.

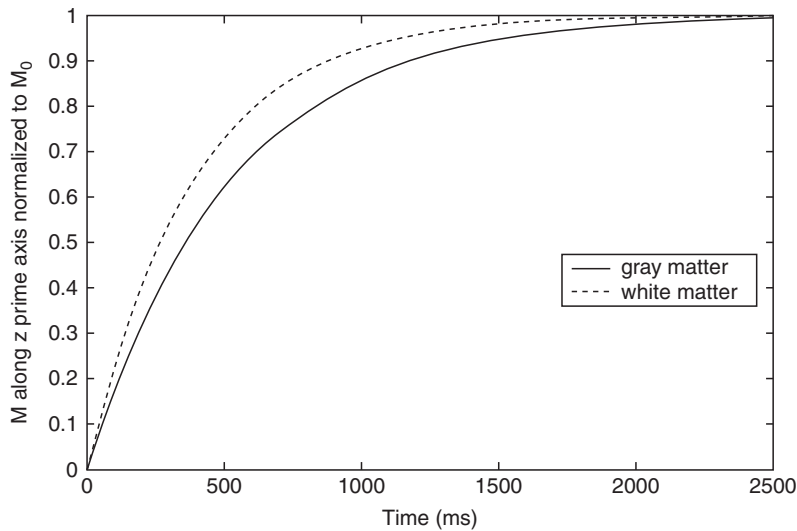


FIGURE 16.51 Longitudinal magnetization versus time for gray matter and white matter.

differences in the T_2^* decay constant, so T_2 weighted images are used. Because these changes are very small, images before and after task initiation are subtracted from each other and the resultant difference image is overlaid on a standard image. Special care must be taken when obtaining these images because the effect is small and can be corrupted by several sources of noise. Typically, hundreds of images are taken for each slice plane position and statistical analysis is used to produce the final image. Sources of noise errors are thermal noise, head movement, and respiratory and cardiac cycles. An example of an fMRI image is shown in Figure 16.52 [5].

Functional MRI has been used extensively to map regions of the brain connected with stimuli, activities, and higher-level cognition. Another example of this type of neuroimaging—biological motion perception—was studied in humans [7]. Subjects were placed in an MRI scanner so they could view moving images while they were being imaged in real-time. Experiments involved biological motion (BM) perception, face recognition, and nonrigid motion (NRM) perception. In Figure 16.53, results from experiments involving these variables are displayed as color-coded regions in three-dimensional reconstructions of a brain. Note the degree of spatial resolution, localization, and discrimination achieved for distinct activities.

16.4 MAGNETOENCEPHALOGRAPHY

Magnetoencephalography (MEG) is a form of neuroimaging that maps the tangential components of magnetic fields associated with scalp potentials produced by the brain [3]. These potentials are the same ones that can be recorded as electroencephalograms (EEGs), but the dynamic magnetic components of these potentials contain different information

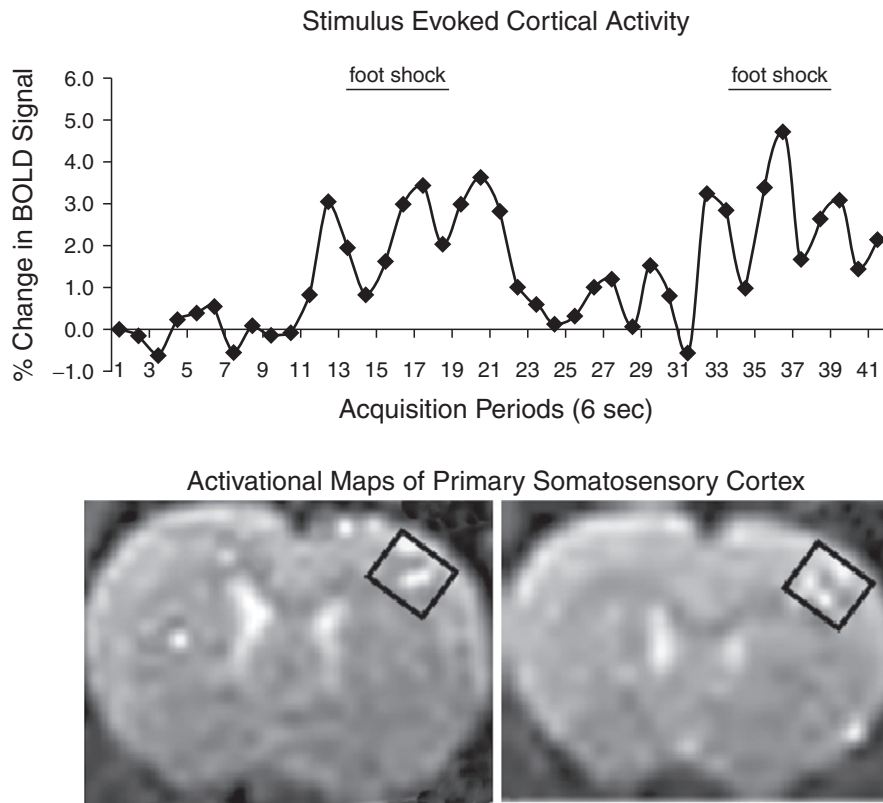


FIGURE 16.52 Functional imaging with fast spin echo. Images show percent change in BOLD signal in the right somatosensory cortex (boxed area in activational maps) in response to electrical stimuli to the left hind limb paw of a rat. From [5], with permission from Elsevier.

with spatial sampling. Unlike fMRI or PET images that provide indirect or delayed clues to synaptic events through changes in the metabolism or blood flow, MEG locates regions of the brain that respond directly to stimuli and yields corresponding time responses at various spatial locations.

To accomplish these tasks, a subject is placed into a helmet-like enclosure that houses a semispherical array of hundreds of magnetic sensing coils. Because the brain's dynamic magnetic field is weaker by five orders of magnitude than magnetic background noise, special noise-suppressing coil configurations, as well as ultrasensitive detectors, superconducting quantum interference devices (SQUIDs), and shielded chambers are needed. The signals from the coils as well as their locations on the semispherical grid are employed in solving the inverse problem of determining the source location of the signals in the brain. These calculations are repeated for different combinations of signals until active regions of the brain are identified with their associated time waveforms. These waveforms are combined with MRI and/or fMRI imaging to aid in localization. A resulting MEG neuroimage is shown in Figure 16.54. In this experiment, parallel localization ("where") and recognition ("what")

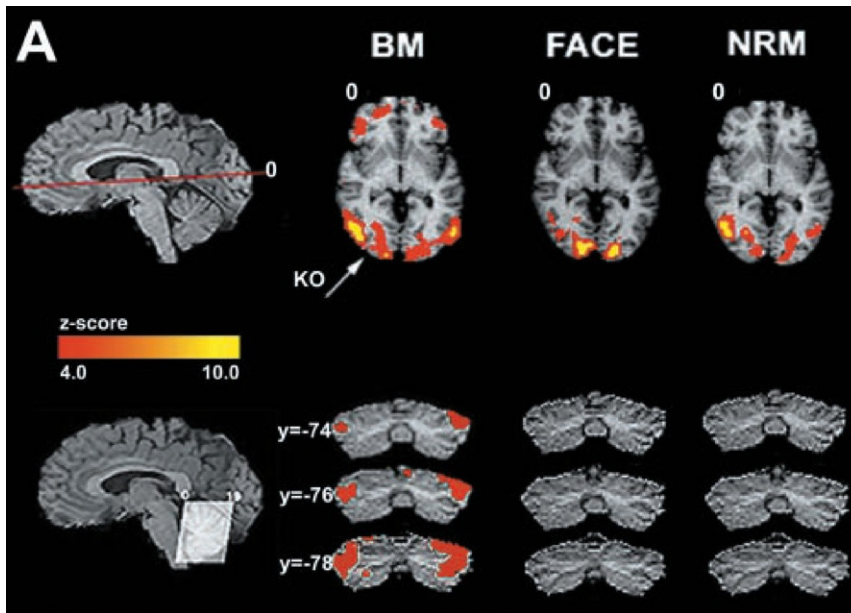


FIGURE 16.53 Example of functional MRI imaging of human brain responses. (A) The grey nearly horizontal line through the top sagittal slice of the brain at the left (denoted by a “0”) shows the position of the three axial slices to the right. On the upper right are group z maps showing statistically significant, group averaged neural activity for each experiment: biological movement (BM), face-gender, and nonrigid motion (NRM). To generate these z maps for each experiment, a t test was performed to contrast each experiment’s task with the control. The grey scale represents the z score of the activation. Note most of the activity is in the KO region and the lateral cerebellum. On the bottom left, the lines through the cerebellum in the sagittal slice indicate the angulation of the coronal cut. To the right, the three coronal slices (arranged vertically) show that only BM had activity in the lateral cerebellum. From [4].

pathways are verified, as well as the ability of a subject to selectively focus attention on either a “where” or “what” aspect. Dipole locations as calculated from received MEG signals on the semispherical grid are indicated on corresponding MRI images.

MEG is used to explore the characteristics of mental patterns such as epilepsy and schizophrenia. It is also useful in brain research to understand cognitive functioning and to learn which parts of the brain are involved in different tasks.

16.5 CONTRAST AGENTS

Contrast agents emphasize or magnify physiological features or functions that would otherwise be invisible, weak, or obscured in images. One of the most frequent applications of these agents is in the vasculature. Another is the uptake of an agent by an organ, indicating a degree of functional or metabolic activity. Each agent is designed to work with the particular physics of the intended imaging modality as well as the region of indication in the body.

16.5.2 Magnetic Resonance Imaging Agents

For MRI, agents distort or alter the magnetic fields locally, where they are concentrated so there is a relative change in a region. The effects achieved can either intensify or weaken the signal close by, depending on the image weighting selected and the context of the agent; they work by reducing T_1 and T_2 relaxation times nearby. The agents tend to be either paramagnetic or supermagnetic materials that are modified to be ingested or infused into the body safely and passed out. The major type of agent used is chelated gadolinium in various forms. The main applications are intravascular and gastrointestinal.

16.5.3 Positron Emission Tomography Agents

For positron emission tomography (PET, introduced in Section 15.3.3), gamma rays are detected that come from a positron-emitting radionuclide material. The location and concentration of these tracer materials in the body are reconstructed from multiple detectors into a 3D image. The tracer most often used is ^{18}F -FDG, a glucose analog. It is concentrations of this substance that are taken up by tissues and indicate local metabolic activity. Only concentrations of this contrast agent are displayed, hanging in space, so it is difficult to determine spatial landmarks to determine locations; therefore, PET images are often combined with another imaging modality such as CT (described in [Section 16.7](#)).

16.5.4 Ultrasound Agents

Ultrasound contrast agents are small microspheres that are used to highlight the passage of blood in regions otherwise difficult to image, such as blood, which is nearly invisible to ultrasound without special processing. These agents are usually microspheres filled with air or gases such as perfluorocarbon, with thin, flexible shells typically made of human serum albumin or surfactants, and are about $4\text{ }\mu\text{m}$ in diameter, similar to the size of red blood cells. They are injected into the venous system to act as blood cell tracers. While in the blood, ultrasound agents significantly improve the ability and sensitivity of ultrasound to follow the flow of blood, especially in small vessels, and the perfusion of blood in muscle, especially those of the heart, and to identify walls of the moving chambers of the heart (opacification). After traveling along in blood, the spheres diffuse and are released as they pass through the lungs.

Ultrasound contrast agents are designed for different applications and effects and are matched to operate at certain insonifying frequencies. They act as miniature nonlinear resonators that greatly enhance their reflectivity for ultrasound. Under certain conditions, the unusual properties of these agents are changes in size, cavitation, fragmentation, or directed movement.

16.6 COMPARISON OF IMAGING MODES

How can imaging modalities be compared? Each major diagnostic imaging method is examined in the following sections, and the overall results are tallied in [Table 16.4](#). Examples of three imaging modalities—CT, MRI, and ultrasound—are shown as different images of the right kidney in [Figure 16.55](#).

TABLE 16.4 Comparison of Imaging Modalities

	Ultrasound	X-ray	CT	MRI
What is imaged	Mechanical properties	Mean tissue absorption	Tissue absorption	Biochemistry (T ₁ & T ₂ , & PD)
Access	Small windows adequate	2 sides needed	Circumferential around body	Circumferential around body
Spatial resolution	Frequency & axially dependent; 3 to 0.3 mm	~1 mm	~1 mm	~1 mm
Penetration	Frequency dependent; 3 to 25 cm	Excellent	Excellent	Excellent
Safety	Very good	Ionizing radiation	Ionizing radiation	Very good
Speed	100 frames per second	Minutes	Half-minute to minutes	Minutes
Cost	\$	\$	\$\$\$\$	\$\$\$\$\$\$\$\$
Portability	Excellent	Good	Poor	Poor

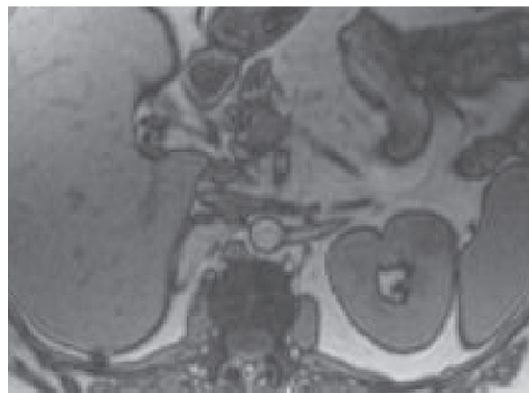
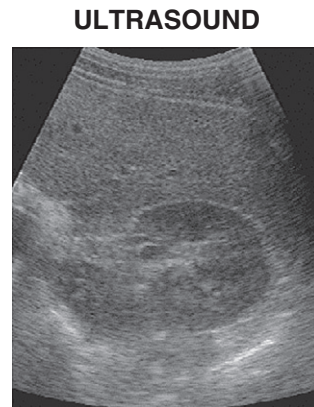
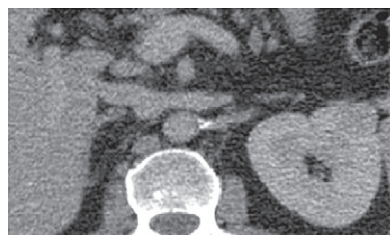
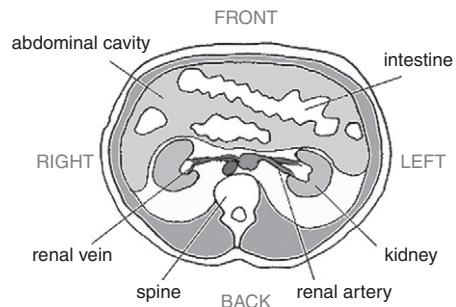
**MRI****ULTRASOUND****CT**

FIGURE 16.55 Images of the right kidney as viewed by different imaging modalities. Upper left: MRI; bottom left: CT; top right: ultrasound; bottom right: graphical depiction of abdominal cross section showing location of kidneys. *Courtesy of Dr. Marilyn Roubidoux.*

16.6.1 Ultrasound

Unlike other imaging modalities, ultrasound resolution and penetration depend on the center frequency and type of transducer selected. The resolution is spatially variant and depends on both the size of the active aperture and the center frequency (and bandwidth) of the transducer and the selected transmit focal depth. A commonly used focal depth to aperture ratio is five, so the half-power beam width is approximately two wavelengths at the center frequency, and thus the transmitted lateral spatial resolution is about two wavelengths. For typical frequencies in use ranging from 1 to 15 MHz, lateral resolution ranges from 3 mm to 0.3 mm and is the smallest in the focal region and varies elsewhere in a nonuniform way because of diffraction effects caused by apertures on the order of a few to tens of wavelengths. For a short pulse, axial resolution is approximately two wavelengths.

Another major factor in determining resolution is attenuation that limits penetration. Attenuation increases with higher center frequencies and depth; therefore, penetration decreases correspondingly, so fine resolution is difficult to achieve at deeper depths.

Ultrasound images are highly detailed and geometrically correct to first-order maps of the mechanical structures of the body according to their “acoustic properties” such as differences in characteristic impedance that depend on stiffness or elasticity and density. The dynamic motion of organs such as the heart can be revealed by ultrasound operating at up to hundreds of frames per second.

Diagnostic ultrasound is noninvasive. Ultrasound is also safe and does not have any cumulative biological side effects. Two other strengths of ultrasound imaging are its relatively low cost and portability. With the widespread availability of miniature portable ultrasound systems for screening and imaging, these two factors will continue to improve.

A high skill level is needed to obtain good images with ultrasound. This expertise is necessary because of the number of access windows, differences in anatomy, the many possible planes of view, and the experience required to find relevant planes and targets of diagnostic significance and to optimize instrumentation. Furthermore, a great deal of experience is required to recognize, interpret, and measure images for diagnosis.

16.6.2 Computed Tomography Imaging

Computed tomography (CT) (also known as computed axial tomography, or CAT) scanning involves x-rays and has been described in Chapter 15. As the x-rays pass through the body, they are absorbed by tissue so an overall “mean attenuation” image results along the ray path. Spatial resolution is not determined by wavelength but by focal spot size of the x-ray tube and scatter from tissue; a typical resolution is about 1 mm. Radioactive contrast agents can be ingested or injected to improve visualization of vessels. Though exposures are short, x-rays are a form of ionizing radiation, so dosage effects can be cumulative and extra precautions are needed for sensitive organs such as the eyes and for pregnancies.

CT equipment is large and stationary so a person can fit inside, and as a result, it is relatively expensive to operate. Consecutive pictures of a moving heart are now achievable through synchronization to ECG signals. The resolution of CT images is typically 1 mm. CT scanning creates superb images of the brain, bone, lungs, and soft tissue, making it complementary to ultrasound.

Although the taking of CT images requires training, it is not difficult. Interpretation of CT cross-sectional images demands considerable experience for a definitive diagnosis.

16.6.3 Magnetic Resonance Imaging

For magnetic resonance imaging, the patient is placed in a strong static magnetic field created by a large enclosing electromagnet. The resolution is mainly determined by the gradient or shape of the magnetic field, and it is typically 1 mm. Images are calculated by reconstruction algorithms based on the sensed voltages proportional to the relaxation times. Tomographic images of cross-sectional slices of the body are computed. The imaging process is fast and reasonably safe, since no ionizing radiation is used. Care must be taken to keep ferromagnetic materials away from the powerful magnets used, and there are limits to the strength of the applied magnetic fields and how quickly they are switched. Because the equipment needed to make the images is expensive, exams are costly.

MRI equipment has several degrees of freedom such as the timing, orientation, and frequency of magnetic fields; therefore, a high level of skill is necessary to acquire diagnostically useful images. Diagnostic interpretation of images involves both a thorough knowledge of the settings of the system and experience.

16.7 IMAGE FUSION

As implied by the comparison of images and the discussion of PET imaging in [Section 16.5.2](#), the physics of each imaging modality reveals different characteristics of tissue properties and functions. In order to obtain a more complete picture, two (or more) imaging modalities can be combined. Image fusion is the simultaneous display of two different types of images either side by side or superimposed. To demonstrate these different points of view, [Figure 16.56](#) compares four types of imaging views of a metastases and is explained next.

One of the leading types of image fusion is PET/CT, where specialized scanners, spatially coregistered, take two sets of images of the same subject in one convenient instrument [2]. As an example, images of a patient with cancer given FDG are shown in [Figure 16.56](#). The top left PET images in frontal and transverse views (A and B) display the uptake of FDG as a small, dark region (see arrow), signifying hypermetabolic activity and the likelihood of a metastases; however, pinpointing the anatomical location of the cancer nodule is ambiguous in these views. The CT view (D), displays good resolution as well as tissue structures but not a clear indication of the nodule. The fusion image (E), a combination of

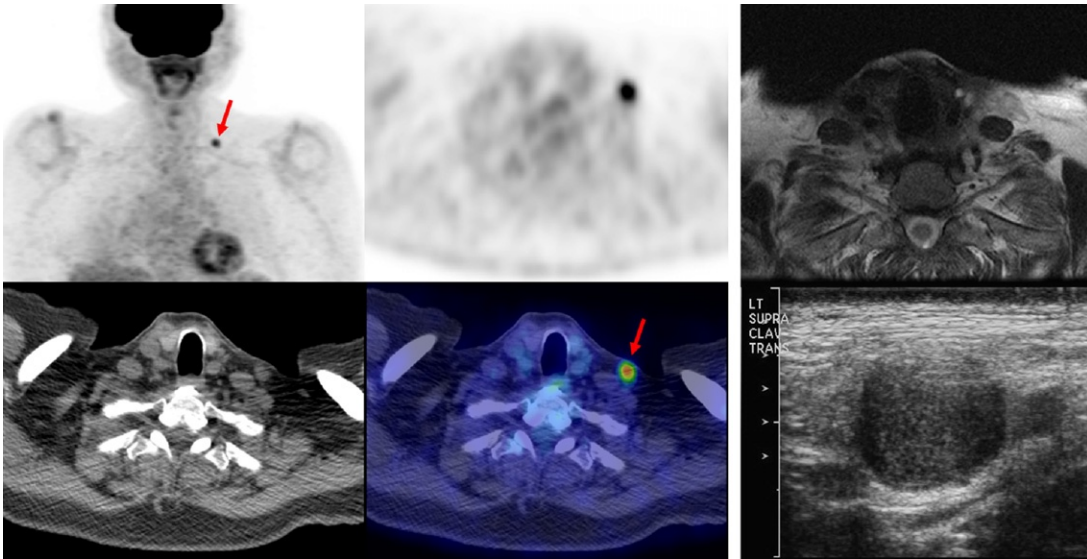


FIGURE 16.56 Images of different imaging modalities. (A) Upper left: PET frontal; (B) upper middle: PET transverse; (C) upper right: MRI transverse; (D) bottom left: CT transverse; (E) bottom middle: PET/CT transverse fused image; and (F) bottom right: ultrasound. Images of a 74-year-old male patient with nasal cavity esthesioneuroblastoma (a form of nasal cancer) who was restaged on a routine follow-up. PET identified a left supraclavicular hypermetabolic nodal metastases (A, B, D, and E) that was not identified in the MRI (C). An ultrasound-guided biopsy of the node was positive for esthesioneuroblastoma and then surgically resected (F). *Courtesy of Dr. Rathan Subramaniam, 2010.*

the PET and CT transverse, clearly emphasizes the metastases. For comparison, the MRI image (C) of the same view, while providing spatial organization of the organs, is by itself not as informative. Finally, the ultrasound image (F) provides a different view and was useful for a guided biopsy.

16.8 SUMMARY

The different features and characteristics of three major imaging modalities are summarized in [Table 16.4](#) and shown in [Figures 16.55](#) and [16.56](#). The tissue properties being imaged are considerably different among the different modalities and can be complementary. Image fusion offers new opportunities to reconcile limitations of individual imaging modalities. Different fusion combinations of imaging modalities have been attempted, but PET/CT fusion is rapidly becoming the most popular [2]. Both CT and MRI can image the whole body with consistent resolution and contrast; however, they are expensive methods of imaging and are slow and not portable. Ultrasound, on the other hand, has high but variable resolution and penetration and limited access to certain portions of the body (intestines, lungs, and bones). It is used to image soft tissues only, but it has the advantages of low cost, portability, and real-time interactive imaging.

16.9 EXERCISES

- Find the Fourier transform of $\prod[(t - t_0)c/L]$ given the Fourier transform pair $\Im[\prod(t)] = \sin(\pi f)/(\pi f) = \text{sinc}(f)$.
- Select the correct answer. Ultrasound imaging for medical applications began to grow significantly when
 - Wild and Reid demonstrated real-time imaging
 - Edler and Hertz started the science of echocardiography
 - Stewart found a connection between cancer in children and prenatal x-ray exposure
 - Satomura and his colleagues detected blood flow using Doppler techniques
- Compute the pressure reflection factor between blood and muscle at normal incidence in dB (use Table 16.1). Compare the reflection factor at 45° incidence to this result. Which is greater?
- Derive the normal reflection and transmission factors in terms of intensity rather than amplitude. Determine the normal transmission intensity factor between blood and (a) the liver, (b) an ideal rigid boundary, and (c) air. How do these compare to the corresponding amplitude results?
- If the Q of the electrical part of a transducer equivalent circuit is defined as $Q = f_0/\Delta f = 1/[\omega_0 C_0 R_A(f_0)]$, where Δf is the -6 dB bandwidth and f_0 is 5 MHz, compare the fractional -6 dB bandwidths (in %) for the following two transducer materials: A $k_T = 0.7$, $\epsilon_R = 1470$ and $k_T = 0.9$ and $\epsilon_R = 680$. (Hint: See Eq. (16.27c).)
- Calculate the electrical impedances of the following two transducer designs at resonance using the constants from Example Problem 16.3: one with a direct water load and one with a matching layer between the crystal and the water load, both with $Z_B = Z_C$. (Hint: Use Eq. (16.34).) What is the improvement in acoustic loss by including the matching layer?
- Ultrasound is not used to image bone directly. (a) To estimate the strength of the reflection, determine the normal amplitude reflection factor from muscle to bone. (b) Determine a matching layer impedance to match the muscle better to bone. (c) What are the amplitude reflection and transmission factors with the matching layer at resonance?
- A company can only afford either a tuning inductor or a matching layer for their transducer product. Which would you recommend and why? Material details: area: $A = 400 \text{ mm}^2$; thickness: $d = 0.87 \text{ mm}$; crystal data: $c = 4.35 \text{ km/s}$; $\epsilon_R^S/\epsilon_0 = 830$; $\epsilon_0 = 8.85 \text{ pF}$; $k_T = 0.49$. Electrical source impedance: $R_g = 50 \text{ ohms}$.
- Compare the frame rates for the following two cases: a 3 MHz cardiac sector scanner with 128 lines per frame for a depth of 10 cm, and a small parts 10 MHz linear array with 300 lines per frame and a 1 cm depth.
- If a 5 MHz transducer in an imaging system has an overall round-trip dynamic range of 100 dB, what is the greatest distance it can detect a pressure reflection between a liver-bone boundary? Between a liver-muscle boundary? Assume average tissue properties to the boundary are the same as that of liver. (Use Table 16.1 for relevant tissue and absorption data.)
- A small lesion about 2 mm in diameter at a depth of 6 cm must be found. Which of the following rectangular array transducers with apertures and center frequencies would you use and why?
 - $L = 15 \text{ mm}$ and 6 MHz
 - $L = 11 \text{ mm}$ and 5 MHz
 - $L = 12 \text{ mm}$ and 3 MHz

Assume $c = 1.5 \text{ mm}/\mu\text{s}$ and a focal length of $F = 60 \text{ mm}$ in the scan plane.

12. For a spherically focusing transducer with an aperture $a = 5$ mm and a frequency of 5 MHz, show which of the following combinations places the effective focal length for a target at a depth of 40 mm.
 - (a) $F = 50$ mm
 - (b) $F = 40$ mm
 - (c) $F = 80$ mm
13. For the Doppler detection of blood, a certain 2 MHz ultrasound system cannot sense signals below a threshold of -35 dB. Assume a layer of muscle with negligible absorption loss above a blood vessel where blood is flowing at a velocity of 1 m/s. Find the range of incident angles (to the nearest degree) that will provide adequate signal strength and the corresponding Doppler frequencies. Use Table 16.1 and note the Doppler angle $= 90^\circ$ —incident angle.
14. For the arrangement of the whirling magnet in Figure 16.29, as d is increased, does the intercepted voltage increase or decrease? What is a physical explanation for this effect? (Note: Volt = Weber/s.)
15. Determine the nuclear magnetic dipole moments, μ_z , for ^1H , ^{19}F , and ^{23}Na . Use Table 16.2.
16. Calculate the net magnetization moment M_0 for water at a temperature of $T = 300^\circ\text{K}$ and a magnetic field of $B_0 = 0.5$ T and a proton density of $N = 6.7 \times 10^{19}$ protons/mm³. Use a form of Eq. (16.54), $\hat{M}_0 = \sum_n \hat{\mu}_n = \hat{\mu}(n_+ - n_-)$ and assume $n_+ = N/2$.
17. If $\hat{B}_y(t) = \hat{y}B_1 \sin(\omega t)$, what will the field be in the rotated frame? After low-pass filtering to eliminate 2ω frequencies, what components are left?
18. (a) For a flip angle of $\pi/2$ radians and $B_1 = 10^{-5}$ T, what is t_p for ^1H ? (b) Find the total flip time for a $\pi/2$ angle followed by a π angle rotation.
19. Determine the relative decay for two individual rotations of $\pi/2$ and π in white matter and a malignant tumor at the time $t = 250$ ms. Which angle provides more contrast between the two tissue types? Repeat at $t = 500$ ms, and compare the contrast to the previous case.
20. (a) Derive an expression for the spectrum of an F. I. D. pulse, $v'(t) = v(t) H(t)$, where $H(t)$ is the step function, $H(t) = 1$ for $t > 0$, and $H(t) = 0$ for $t < 0$. Utilize the Fourier transform pair, $\Im[e^{-a|t|}H(t)] = \frac{1 - i2\pi f/a}{|a|[1 + (2\pi f/a)^2]}$. (b) What is the complex ratio of the F.I.D. spectrum to that of the spin echo? (c) Find the value of this ratio at the Larmor frequency. (d) Can you find an explanation for this ratio based on the time waveforms involved?
21. (a) If $T_2 = T_2^* = 5$ ms for the F. I. D. pulse of problem 20, find the spectral component at the Larmor frequency of 5 MHz for the conditions $B_1 = 20 \mu\text{T}$, $I = 1$ A, $V_{\text{oxel}} = 1 \text{ cm}^3$, and $M_{xy}^0 = 5 \times 10^{-12} \text{ J}/(\text{T}\cdot\text{mm}^3)$. (b) How does this value compare for a similar spectral magnitude of a spin echo with T_2 for fat at the same Larmor frequency?
22. Find the -6 dB width of the envelope of a time pulse and the two end frequencies needed to scan a 1-mm-thick slice from -15 cm to $+15$ cm around an isocenter on the z -axis. Assume $G_z = 0.5 \text{ T/m}$.
23. (a) In order to cover a range of ± 10 cm about an isocenter along the y -axis, phase encoding is applied with a pulse length $t_p = 10 \mu\text{s}$ for ^1H and an overall phase shift of $\pi/2$. Find the slopes, G_{ym} , at the end points and the slope resolution for 256 steps.

Continued

24. Determine the relative position (x_n, y_m) from the center for ^1H , given $f_n = 78.5 \text{ MHz}$, $G_x = 10^{-4} \text{ T/m}$, $t_p = 5 \mu\text{s}$, and $u_m = 21.3 \text{ m/T}$.
25. Derive $s_{nm}(k_x, k_y)$ based on Eq. (16.87).
26. Answer the following:
 - (a) What is displayed in an MRI image?
 - (b) How is a location from a set of signals in the body determined?
 - (c) Of the three imaging axes, which are actively controlled and which are passively sensed?
27. Explain the basic physical principles underlying the differences in appearance (image content, and tissue differentiation) among T_1 , T_2 , and PD weighted images.
28. What are the complementary aspects of PET and CT images that make them suitable for image fusion?

References

- [1] J. Ahveninen, et al., Task-modulated “what” and “where” pathways in the human auditory cortex, *Proc. Natl. Acad. Sci. U. S. A.* 103 (2006) 14608–14613.
- [2] T.M. Blodgett, C.C. Meltzer, D.W. Townsend, PET/CT: Form and Function, *Radiology* 242 (2007) 360–385.
- [3] D. Cohen, E. Halgren, Magnetoencephalography, *Encyclopedia of Neuroscience* 5 (2009) 615–622.
- [4] P.C. Lauterbur, Image formation by induced local interactions: Examples employing nuclear magnetic resonance, *Nature* 242 (1973) 190–191.
- [5] R. Ludwig, G. Bodgdanov, J. King, A. Allard, C.F. Ferris, A dual Rf resonator system for high-field functional magnetic resonance imaging of small animals, *J. Neurosci. Methods* 132 (2004) 125–135.
- [6] R.K. Panda, Development of novel piezoelectric composites by solid freeform fabrication techniques, Dissertation, Rutgers, New Brunswick, NJ, 1998.
- [7] L.M. Vaina, J. Solomon, S. Chowdhury, P. Sinha, Belliveau, Functional neuroanatomy of biological motion perception in humans, *Proc. Natl. Acad. Sci. U. S. A.* 98 (2001) 11658–11661.

Suggested Readings

- F. Bitter, H.A. Medicus, *Fields and Particles: An Introduction to Electromagnetic Wave Phenomena and Quantum Physics*, American Elsevier, New York, 1973.
- D.W. Chakeres, P. Schmalbrock, *Fundamentals of Magnetic Resonance Imaging*, Williams & Wilkins, Baltimore, MD, 1992.
- Z.H. Cho, J.P. Jones, M. Singh, *Foundations of Medical Imaging*, Wiley, New York, 1993.
- J.A. Jensen, *Estimation of Blood Velocities Using Ultrasound*, Cambridge Univ. Press, Cambridge, 1996.
- E.E. Kim, E.F. Jackson, *Molecular Imaging in Oncology*, Springer-Verlag, Berlin, 1999.
- G.S. Kino, *Acoustic Waves: Devices, Imaging, and Analog Signal Processing*, Prentice-Hall, Englewood Cliffs, NJ, 1987.
- V. Kuperman, *Magnetic Resonance Imaging Physical Principles and Applications*, Elsevier Academic, Boston, 2000.
- Z.P. Liang, P.C. Lauterbur, *Principles of Magnetic Resonance Imaging: A Signal Processing Approach*, IEEE Press, New York, 2000.
- K.K. Shung, M.B. Smith, B.M.W. Tsui, *Principles of Medical Imaging*, Academic, San Diego, CA, 1992.
- T.L. Szabo, 1998, Transducer arrays for medical ultrasound imaging, in: A. Duck, A.C. Baker, H.C. Starritt (Eds.), *Ultrasound in Medicine*, Medical Science Series, F, Institute of Physics Pub., Bristol, UK.
- T.L. Szabo, *Diagnostic Ultrasound Imaging: Inside Out*, Elsevier Academic, Boston, 2004.